DESIGN-DRIVEN PERFOMANCE ENHANCEMENTS OF SUPERCONDUCTING FLUX QUBITS

ORIOL DE MIGUEL RIBAS

Institut de Física d'Altes Energies

Universitat Autònoma de Barcelona

Tutored by Dr. Pol Forn-Díaz with
Dr. Ramón Muñoz Tapia as academic tutor

Facultat de Ciències at Universitat
Autònoma de Barcelona (UAB)

Physics BSc. Undergraduate Thesis to obtain the Degree in Physics

Bellaterra, September 2024

DECLARACIÓ D'AUTORIA DEL TREBALL DE GRAU

Jo, Oriol De Miguel Ribas, amb DNI 49222447D, i estudiant del Grau en Física de la Universitat Autònoma de Barcelona, en relació amb la memòria del treball de final de Grau presentada per a la seva defensa i avaluació durant la convocatòria de Setembre del curs 2023-2024, declara que

- El document presentat és original i ha estat realitzat per la seva persona.
- El treball s'ha dut a terme principalment amb l'objectiu d'avaluar l'assignatura de treball de grau en física en la UAB, i no s'ha presentat prèviament per ser qualificat en l'avaluació de cap altre assignatura ni aquesta ni en cap altre universitat.
- En el cas de continguts de treballs publicat per terceres persones, l'autoria està clarament atribuïda, citant les fonts degudament.
- En el casos en els que el meu treball s'ha realitzat en col·laboració amb altres investigador i/o estudiants, es declara amb exactitud quines contribucions es deriven del treball de tercers i quines es deriven de la meva contribució.
- A l'excepció del punts esmentats anteriorment, el treball presentat es de la meva autoria.

Bellaterra, Setembre 2024

ORIOL DE MIGUEL RIBAS - DNI 49222447D

Firmado digitalmente por ORIOL DE MIGUEL RIBAS - DNI 49222447D
Fecha: 2024.07.31 12:48:33 +02'00'

Oriol De Miguel Ribas

DECLARACIÓ D'EXTENSIÓ TREBALL DE GRAU

Jo, Oriol De Miguel Ribas, amb DNI 49222447D, i estudiant del Grau en Física de la Universitat Autònoma de Barcelona, en relació amb la memòria del treball de final de Grau presentada per a la seva defensa i avaluació durant la convocatòria de Setembre del curs 2023-2024, declara que:

- El nombre total de paraules incloses en les seccions des de la introducció a les conclusions es de 7192 paraules
- El nombre total de figures es de 12.

En total el document, comptabilitza:

$$7192 \text{ paraules} + 12 \times 200 \text{ paraules/figura} = 9992$$

Que compleix amb la normativa al ser inferior a 10000.

Bellaterra, Setembre 2024

ORIOL DE MIGUEL RIBAS - DNI 49222447D

Firmado digitalmente por ORIOL DE MIGUEL RIBAS - DNI 49222447D
Fecha: 2024.07.31 12:48:57 +02'00'

Oriol De Miguel Ribas

DECLARACIÓ SUPERVISIÓ TREBALL DE GRAU

Aquest document té com a objectiu certificar que l'alumne Oriol De Miguel Ribas, amb DNI 49222447D, ha realitzat el seu treball titulat "Design-driven perfomance enhancements of superconducting flux qubits" sota la meva direcció, i el presentarà per tal de defensar l'assignatura a Treball final de grau en el Grau de Física.

L'alumne m'ha fet arribar el formulari word d'avaluació de l'activitad de l'alumne per part del director.

Nom del director: Dr. Pol Forn-Díaz

Institució a la que pertany: IFAE

Bellaterra, Setembre 2024

Director del Treball

ABSTRACT

This thesis introduces Superconducting Qubits as a platform for Quantum Computing. It also explains the theory needed to study and understand these circuits, highlighting the use of Circuit QED Theory to obtain their Hamiltonian. The main idea is to make the physical circuit more complex to enhance its properties. The attribute highlighted in this work is coherence time, which corresponds to the time during which the qubit stays in a well-defined quantum state. Different circuits that show longer coherence times are presented and their parameters are optimized. Moreover, the main decoherence mechanism is identified by means of *ScQubits* simulations and different strategies are presented in order to minimize its effect.

Furthermore, the concept of linear quantum crosstalk is introduced and its appearance in the Hamiltonian is justified. The implications that this effect has on the potential energy, coherence time and frequency of the qubit are studied. This thesis also presents more complex circuit geometries capable of vanishing linear quantum crosstalk. The elimination of this effect improves the controlability of the system, giving the researcher the ability to tune independently different parameters of the Hamiltonian.

The role of parameter asymmetry is presented and compared in two circuit configurations. This thesis shows how asymmetry leads to nonlinear quantum crosstalk and how it alters the Hamiltonian of the qubit. Special emphasis is put on the deviations caused by low asymmetry.

This thesis culminates on the proposition of a qubit geometry which unifies the best features of the different circuits studied. Nevertheless, this superconducting circuit is not studied in detail and, therefore, could be a promising continuation to this line of work.

CONTENTS

1 INTRODUCTION 1
- 1.1 Introduction to Quantum Computing 1
- 1.2 Qubits and Superconducting Circuits 1
- 1.3 Advantages and disadvantages of Superconducting Circuits as qubits 3

2 OBJECTIVES 5

3 THEORETICAL BACKGROUND 7
- 3.1 Introduction to circuit QED Theory 7
- 3.2 Circuit elements 8
- 3.3 Coherence time 10

4 SUPERCONDUCTING QUBITS 11
- 4.1 C-shunted N-Josephson Junction Flux Qubit 11
  - 4.1.1 The double-well potential and a necessary condition for a N-Josephson Junction Flux Qubit . 13
- 4.2 The RF-SQUID 14
- 4.3 3JJ Flux Qubit with tunable asymmetric X loop 14
  - 4.3.1 Coherence time dependencies of the 3JJ Flux Qubit 17
  - 4.3.2 Effects of the asymmetry on the potential 18
- 4.4 The Fluxonium limit 19
  - 4.4.1 Coherence time of the Fluxonium Qubit 21
- 4.5 Gradiometric Flux Qubit 22
  - 4.5.1 Double well potential for the asymmetric gradiometric flux qubit 23
- 4.6 Possible continuation of this work 25

5 CONCLUSIONS 27

A APPENDIX 29
- A.1 In-depth deduction of the NJJ Hamiltonian 29
- A.2 In-Depth deduction of the RF-SQUID Hamiltonian . . 30
- A.3 Intermediate steps towards 3-Josephson Junction potential 30
- A.4 Intermediate steps towards the Gradiometric Qubit potential 31
- A.5 Verification of the Gradiometric Qubit potential 32
- A.6 Code used 33

BIBLIOGRAPHY 49

LIST OF FIGURES

Figure 3.1 Diagrams of circuit elements. 8
Figure 4.1 Diagrams of a C-Shunted N Josephson Junction Flux Qubit. 11
Figure 4.2 Double-well potential. 13
Figure 4.3 Diagram of a 3 Josephson Junction Flux Qubit. 15
Figure 4.4 Potential energy of a 3 Josephson Junction Flux Qubit. 16
Figure 4.5 Effective relaxation time for the 3 Josephson Junction Qubit. 18
Figure 4.6 Qubit frequency as a function of external fluxes. 18
Figure 4.7 Fluxonium potential and wavefunctions of the first eigenstates. 19
Figure 4.8 Flux drop and intensity for the Fluxonium Qubit. 20
Figure 4.9 Coherence time associated to the inductance and the position of the well. 21
Figure 4.10 Diagram of a Gradiometric Flux Qubit. 22
Figure 4.11 Potential for the asymmetric gradiometric circuit. 24

LISTINGS

Listing A.1 General initialization of the code 33
Listing A.2 Graphical representation of the double-well potential of the 3-Josephson Junction Flux Qubit. 34
Listing A.3 Graphical representation of the potential of the 3-Josephson Junction Flux Qubit. 35
Listing A.4 Simulation to find the predominant noise mechanism. 36
Listing A.5 Power law between the effective relaxation time and the frequency of the qubit. 37
Listing A.6 Coherence time as a function of E_J. 38
Listing A.7 Coherence time as a function of E_J/E_C. 39
Listing A.8 Coherence time as a function of the distance to the double well limit. 40
Listing A.9 Coherence time as a function of external fluxes for a symmetric and asymmetric 3-Josephson Junction Flux Qubit. 41

Listing A.10 Potential of the Fluxonium and representation of the wavefunctions of the lowest eigenstates. 42
Listing A.11 Minima of the double well for the Fluxonium. 43
Listing A.12 Expectation value of the Intensity of the Fluxonium as a function of N. 44
Listing A.13 Part I: Simulation of coherence time for the Fluxonium circuit. 45
Listing A.14 Part II: Simulation of coherence time for the Fluxonium circuit. 46
Listing A.15 Single-variable potential of asymmetric gradiometric qubit. 47
Listing A.16 Single-variable potential of asymmetric gradiometric qubit for different asymmetry values. . 48

ACRONYMS

PCQ Persistent-Current Qubit
RF-SQUID Radio Frequency Superconducting Quantum Interference Device

1 INTRODUCTION

1.1 INTRODUCTION TO QUANTUM COMPUTING

It is undeniable that digital computation has shaped the society that we live in, becoming the base of the Information Era and the driving force behind the Fourth Industrial Revolution [1]. However, the reduction of size of transistors, a key element in the digital revolution, is reaching its physical limitations and some experts are already declaring Moore's experimental Law [2] as dead. Considering both the predicted digital decay and inherent limitations to solve relevant NP-hard problems, there is a need for a new type of computation. Taking advantage of the deep understanding of Quantum Mechanics and Information Theory, Benioff [3] theorized and published a lattice system of spins equivalent to a Turing Machine. In other words, he proposed a quantum system that was able to compute via unitary matrix evolution, which is the cornerstone of Quantum Mechanics. The idea of constructing a Quantum Computer based on unit blocks that were coupled to each other began to take root, until a few years later DiVincenzo [4] proved that quantum gates which operate on two qubits are sufficient to construct a general quantum circuit. A **qubit**, or quantum bit, is the fundamental unit of quantum information. Systems built from qubits have a very broad range of applications in quantum communication [5, 6], quantum simulation [7, 8], quantum computing [9, 10] and quantum cryptography [11–13].

1.2 QUBITS AND SUPERCONDUCTING CIRCUITS

Generally, a physical system consists of multiple quantum states. If we constrain the Hilbert space to the one spanned by two states, then this system could behave as a qubit. The most important requierements for a qubit [14] are the following: the qubit has access to the Hilbert space spanned by two orthogonal eigenstates, projective measurements and unitary operations can be implemented on the qubit and the qubit can be reset to a given initial state. In addition, building an operational quantum computer requires controllable qubit-qubit interactions. From a practical perspective, a qubit should have a coherence time, *i.e.* the time during which the qubit stays in a well-defined quantum state, longer than the computational time needed for a certain protocol, such as a quantum algorithm.

The coherence time is heavily influenced by the coupling between the qubit and its environment. The main decoherence processes are the dissipation of energy, heating by external fluctuations and dephasing of eigenstates leading to random fluctuations of the qubit frequency. These are the reasons why a qubit has to be as isolated as possible from its environment to maintain superpositions and entanglement. Furthermore, the system has to be at very low temperatures (in the range of the mK for superconducting circuits). These values correspond to the quantum regime ($h\nu \gg k_b T$), with ν the characteristic frequency of the qubit. The reason behind is that the qubit tends to a state in thermal equilibrium with the environment. If the system is not in the quantum regime, thermal fluctuations become non-negligible and overrun quantum fluctuations.

A considerable number of physical systems may behave as qubits: photons using their polarization or frequency, electrons using their spin or position in two quantum wells [15], nuclei with their angular momentum [16], atoms [17], ions [18], color centers [19] and molecules [20]. However, in this thesis the system that Orlando [21] proposed is studied: the Persistent-Current Qubit (PCQ).

Roughly speaking, a superconducting circuit is a circuit constructed with superconducting materials. A circuit exhibits *quantum phenomena* when it behaves as a quantum system. These properties are energy quantization, entanglement via hybridization of quantum states, unitary evolution and quantum superposition. All these properties are exhibited through quantum observables such as magnetic flux, charge, electric current and voltage. A commonly used strategy is to map a microscopic and quantized degree of freedom to a macroscopic one that is easier to measure. In the case at study, PCQ's orthogonal eigenstates correspond to current flowing clockwise and counterclockwise.

Because of the non-linearity of the circuit components used to build PCQs, these circuits exhibit an anharmonic energy spectrum. Therefore, the energy of the transition between the ground state $|0\rangle$ and first excited state $|1\rangle$ is not related by an integer to the transitions to the rest of eigenstates and the subspace made from its combination becomes isolated. Thus, the circuit behaves as an artifical two-level atom.

1.3 ADVANTAGES AND DISADVANTAGES OF SUPERCONDUCTING CIRCUITS AS QUBITS

On the one hand, PCQ's flexibility allows to change the Hamiltonian of the system just modifying parts of an electrical circuit. Therefore, in the bigger picture, the advantages that this approach offers are the scalability of the system and the tunability of its components both at fabrication and via external magnetic fluxes.

On the other hand, one of the few disadvantages of PCQ versus other quantum computers, such as Rydberg atoms [22], is that each element of the circuit is not identical. Therefore, the effects on the potential of the system caused by slightly different circuit components should be considered. Nevertheless, PCQ's biggest disadvantage is decoherence.

2 OBJECTIVES

The main objective of this thesis is to gain a better understanding of how a superconducting qubit works in order to optimize it. Specifically, this thesis aims to enhance the qubit in the following areas: improving its coherence time, understanding quantum crosstalk to correct it, and studying the effects of junction asymmetry. More specifically, the objective is to make the physical qubit more robust by simplifying its Hamiltonian. This should result in better properties such as longer coherence times and greater control of the qubit.

The specific objectives are the following:

- Utilize circuit QED Theory to obtain the Hamiltonians of different circuits.
- Understand qubit decoherence and noise and how to minimize it.
- Determine the effects of having N big Josephson Junctions in a qubit and how it relates to the Fluxonium qubit limit.
- Understand the effects of Quantum Crosstalk and the need to calibrate it in order to operate the qubit.
- Model analytically the asymmetry of junctions to understand its effects on the potential energy of the qubit.

Moreover, this thesis has another objective which is not directly linked to the main one:

- Act as an introduction to the field of Quantum Hardware and serve as a guide for the reader to build fundamental knowlegde about PCQs.

3 THEORETICAL BACKGROUND

The objective of this Chapter is to provide the necessary review of the theory to mathematically model the dynamics of a superconducting qubit through its Hamiltonian. Special emphasis has been given to the coherence time due to the key role that plays in quantum computing. This chapter is built from the original Quantum network theory from Yurke and Denker [23], the course from Devoret [24], the lecture from Girvin at the Quantum Machines Summer School of Les Houches [25], the book of García-Ripoll [14] and the in-depth explanations of Wendin and Shumeiko's review [26].

3.1 INTRODUCTION TO CIRCUIT QED THEORY

The dynamics of a system are encompassed in its Hamiltonian and the properties of the system can be predicted through the analysis of this mathematical object. This section defines a method that consistently builds Hamiltonians from known solutions in the form of a set of differential equations, which are found using the classical Kirchoff's Laws.

First of all, each circuit element "breaks" the circuit in 2 separate nodes. All distinct nodes of the circuit have an associated flux variable Φ_j. A branch is defined as the connection between two consecutive nodes. Then, a difference flux $\Phi_{j-i} \equiv \Phi_j - \Phi_i$ is associated to each branch. The first quantum effect of the circuit is fluxoid quantization [27, 28]: for each closed loop the total number of fluxoids must be proportional to an integer number of flux quanta $\Phi_0 := \frac{h}{2e}$. A closed loop that is thread by an external flux Φ_{ext} and is formed by the set of $\{\alpha_i\}$ branches must satisfy:

Notice that a branch flux equals to the phase drop across a circuit element.

$$\sum_{\{\alpha_i\}} \Phi_i + \Phi_{ext} = n\Phi_0. \tag{3.1}$$

Once the branch fluxes are defined and the fluxoid quantization is applied, Kirchoff's Laws can be used via current conservation for each node. This process yields a set of differential equations which are solution to the Euler-Lagrange Eqs. of motion (3.2) for all flux variables:

Via fluxoid quantization, inherent degrees of freedom can be "swapped" by tunable external fluxes.

$$\frac{\partial \mathcal{L}}{\partial \Phi_i} - \frac{d}{dt}\frac{\partial \mathcal{L}}{\partial \dot{\Phi}_i} = 0. \tag{3.2}$$

Given the Lagrangian density $\mathcal{L}$, the node charges q_i are found as the canonically conjugate momenta of the fluxes, using $q_i = \frac{\partial \mathcal{L}}{\partial \dot{\Phi}_i}$. Then, the Hamiltonian is found using the Legendre transformation:

$$\mathcal{H}(\mathbf{\Phi}, \mathbf{q}) = \sum_i q_i \dot{\Phi}_i - \mathcal{L}(\mathbf{\Phi}, \dot{\mathbf{\Phi}}). \tag{3.3}$$

In order to obtain the Hamiltonian as a proper quantum operator, the canonical variables are promoted to canonical operators which satisfy the commutation relations:

$$[\widehat{\Phi}_i, \widehat{q}_j] = i\hbar\delta_{ij}, \tag{3.4}$$

where i is the imaginary unit, $\hbar$ is the reduced Plank constant and δ_{ij} is the Kronecker delta. Using this procedure, the Hamiltonian of any PCQ can be obtained. The only ingredient missing is the relation between the magnetic flux and the current intensity $I(\Phi)$, which is *circuit-element* dependent and is explained in the following section.

3.2 CIRCUIT ELEMENTS

This section contains a brief explanation of the building blocks of a PCQ: capacitors, inductors and Josephson Junctions. These circuit elements are gathered in Figure 3.1. Since we consider the size of the circuit elements to be much smaller than the wavelength of the current and voltage oscillations[1], the lumped-element circuit approximation [29] can be applied. In this regime, both current and voltage have no spatial dependance and the circuit elements can be treated like a point.

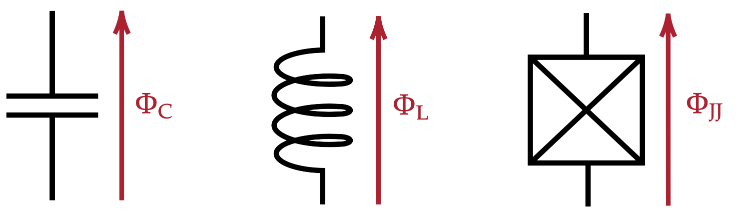

(a) Capacitor. (b) Inductor. (c) Josephson Junction.

Figure 3.1: Diagrams of circuit elements.

CAPACITOR 3.1A: Classically, a capacitor consists of two plates which accumulate charge of opposite sign. Therefore, an electric field

1 These oscillations are of the order of microwaves, which correspond to wavelenghts in the range of centimeters.

is generated which is proportional to the charge stored. The differential form of this relation corresponds to equation $I = C\frac{dV}{dt} = C\ddot{\Phi}$, where C is the capacitance.

Work needs to be done in order to charge the capacitor, which is stored as electrostatic energy. If the capacitor is a superconductor, then the energy $E = 4E_C n^2$ will depend on the number of extra Cooper pairs n that are stored in the capacitor and on the characteristic capacitive energy $E_C = \frac{e^2}{2C}$, with e the charge of an electron.

Since the charge of the capacitor is $q = -2en$, when the charge and the flux are promoted to operators in the quantization procedure, the number of Cooper pairs is promoted to a number operator with $\widehat{q} = -2e\widehat{n}$. Thus, a capacitor will add $\widehat{\mathcal{H}}_{cap} = \frac{C_a}{2}\widehat{\dot{\Phi}}_a^2 = \frac{\widehat{q}_a^2}{2C_a} = 4E_{C_a}\widehat{n}_a^2$ to the Hamiltonian.

INDUCTOR 3.1B: Classically, the inductor is a circuit element that acts as a magnetic flux inertia. The relationship between its current intensity and flux corresponds to $I = \frac{\Phi}{L}$, where L is the inductance of the inductor. Since it resists to changes in its magnetic flux, work has to be done in order to change this variable and it stores magnetic energy, which is proportional to the magnetic flux.

Using superconducting materials adds kinetic inductance [21], which affects the value of L. In the quantization procedure, the magnetic flux promotes to an operator and, therefore, an inductor will add the term $\widehat{\mathcal{H}}_{ind} = \frac{1}{2L_i}\widehat{\Phi}_i^2$ to the Hamiltonian.

JOSEPHSON JUNCTION 3.1C: The Josephson Junction stands out because its behaviour is purely quantum mechanical. Roughly, a Josephson Junction consists of two superconductors separated with an insulator such that Josephson Tunneling can occur. This effect, which was predicted by Josephson [30], reaffirmed by Anderson and Rowell [31] and later confirmed by Giaever [32], consists of the tunneling from one superconductor to the other of the whole macroscopic wavefunction of the two superconductors on each side. This results in a coherent coupling between the two superconductors and the existence of a relative phase $\varphi_i = \frac{2\pi}{\Phi_0}\Phi_i$ between them, with Φ_i being the effective magnetic flux across the junction.

This effect has been widely studied (see [33, 34]) but only the properties that are useful for PCQ will be discussed. In the lumped element approximation, the current intensity flowing through a Josephson Junction corresponds to the equation $I = I_C \sin\varphi_i$, with I_C the critical current of the Josephson Junction. The critical current corresponds to the maximum value of current intensity in which the system has a flow of electrical supercurrent without a voltage drop.

Considering that a Josephson Junction also has capacitive energy, after the quantization procedure its contribution to the Hamiltonian corresponds to $\widehat{\mathcal{H}}_{JJ} = \frac{\widehat{q}_i^2}{2C_J} - E_J \cos\left(\frac{2\pi}{\Phi_0}\widehat{\Phi}_i\right)$, where $E_J = I_C\Phi_0/2\pi$ is the characteristic Josephson energy.

For small currents, a Josephson Junction can be considered a tunable inductor with inductance $L_J = \Phi_0 \Big/ 2\pi I_C\sqrt{1-\left(\frac{I}{I_C}\right)^2}$. It is also worth to state that I_C depends on the size of the Josephson Junction, making this circuit element adjustable by design. Also, a Josephson Junction is highly sensitive to external magnetic fluxes.

The terms of the Hamiltonian which depend on the magnetic fluxes $\mathbf{\Phi}$ can play the role of a potential $U(\mathbf{\Phi})$. In the Josephson Junction's case and due to the cosine, for small fluxes ($\varphi \ll 1$) this potential will be harmonic to first order. Nevertheless, as φ increases, more corrections are added. Therefore, the Josephson Junction generates an anharmonic potential that isolates the ground state and the first excited from the rest of the eigenstates, which defines a PCQ, and gives the ability to the researcher to tune parameters of the Hamiltonian of the system via external fluxes.

3.3 COHERENCE TIME

Derived from time-dependent perturbation theory, it was first formulated by Dirac [35, 36] and gained its importance due to Fermi [37].

Fermi's Golden Rule (3.5) is typically used to estimate the coherence time of a qubit. This equation describes the transition rate from an initial state i to a final state f and the relaxation time is obtained as the inverse of the transition rate $\Gamma_{1i\to f}$:

$$\frac{1}{T_1} \equiv \Gamma_{1i\to f} = \frac{1}{\hbar^2}|\langle f|\widehat{\mathcal{H}}'|i\rangle|^2 S(\omega_{if}); \quad \frac{1}{T_2} \equiv \Gamma_{2i\to f} = \frac{\Gamma_{1i\to f}}{2} + \Gamma_\phi. \quad (3.5)$$

Therefore, the relaxation time depends on the matrix element of the Hamiltonian $\widehat{\mathcal{H}}'$ of the decoherence mechanism and the noise power spectral density $S(\omega_{if})$ associated to the frequency ω_{if}. To be precise, T_1 corresponds to the lifetime of the qubit, whereas coherence time is defined as T_2 using Eq. (3.5). Therefore, the coherence time depends both on the lifetime of the state of the qubit and on the pure dephasing rate Γ_ϕ, which makes the qubit frequency fluctuate and effectively reduces the coherence time of the qubit. As justified in [38], if the qubit is driven under certain conditions of external flux, pure dephasing may be corrected. For simplicity, these conditions have been used on the simulations and, thus, the tendencies of T_1 determine the tendencies of the coherence time.

When different decoherence mechanisms are considered, the inverse effective relaxation time depends on $\frac{1}{T_{1\text{eff}}} = \frac{1}{2}\sum_i \frac{1}{T_{1i}}$, where T_{1i} is the relaxation time from the ith decoherence mechanism.

4 SUPERCONDUCTING QUBITS

This Chapter contains the body of the work carried out in this thesis. We study several superconducting qubits by analyzing the advantages and disadvantages, from the Radio Frequency Superconducting Quantum Interference Device (RF-SQUID) to the asymmetric Gradiometric Qubit. With each iteration, the circuit becomes physically more sophisticated but contains more design-driven performance enhancements, implying in longer coherence times and more controlability. Even though it may seem counter-intuitive, this Chapter starts with the deduction of the Hamiltonian of a generalized circuit and includes a generalized proof for the conditions required to display a double well. Then, more specific and simpler cases are studied improving an aspect of the qubit in each iteration.

4.1 C-SHUNTED N-JOSEPHSON JUNCTION FLUX QUBIT

The generalized case of a Flux Qubit is made of N big Josephson Junctions in series which are connected to a smaller Josephson Junction (with a ratio of physical area of α). The α-Junction is also connected in parallel to a capacitance, as it can be seen in Figure 4.1a.

The characteristic energies of a Josephson Junction depend on its physical size. A ratio of α implies in a Josepshon energy of αE_J and a charging energy of E_C/α.

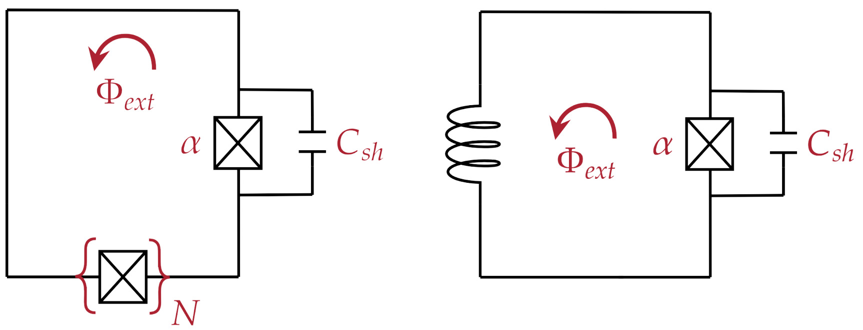

(a) General diagram.

(b) Equivalent diagram in the Fluxonium limit.

Figure 4.1: Diagrams of a C-Shunted N Josephson Junction Flux Qubit.

To find the Hamiltonian of the system, the nodes have to be identified. Node 1 can be arbitrarily placed between the α-Junction and the first big Josephson Junction. Node 2 can be placed between the first and second big Josephson Junction and this process can be repeated until the node $N+1$, which is placed between the N Junctions and the α-Junction. The branch nodes are $\Phi_{JJi} = \Phi_i - \Phi_{i-1}$ for the big Junctions and $\Phi_{JJ\alpha} = \Phi_1 - \Phi_{N+1}$ for the α-Junction. Since the number of fluxoids is quantized, all branch fluxes are related to each other and to the external flux with $\sum_{i=i}^{N} \Phi_{JJi} + \Phi_{JJ\alpha} + \Phi_{ext} = n\Phi_0$.

In this case, it is useful to apply fluxoid quantization for the branch flux of the α-Junction. Therefore, applying Kirchoff's Laws and the relations $\Phi = f(I)$ of Sec. 3.2, the system must obey:

$$\begin{aligned} C_J \ddot{\Phi}_{JJi} + I_C \sin \varphi_{JJi} &= C_J \ddot{\Phi}_{JJi+1} + I_C \sin \varphi_{JJi+1} \\ C_J \ddot{\Phi}_{JJN} + I_C \sin \varphi_{JJN} &= (\alpha C_J + C_{sh}) \ddot{\Phi}_{JJ\alpha} + \alpha I_C \sin \varphi_{JJ\alpha}. \end{aligned} \tag{4.1}$$

The Lagrangian of the system is obtained integrating Eqs. (4.1) with respect to time and knowing that they all obey Eq. (3.2):

$$\begin{aligned} \mathcal{L} = \sum_{i=1}^{N} \frac{C_J}{2} \dot{\Phi}_{JJi}^2 + \frac{\alpha C_J + C_{sh}}{2} \left(\sum_{i=1}^{N} \dot{\Phi}_{JJi} \right)^2 \\ + \sum_{i=1}^{N} E_J \cos \left(\frac{2\pi}{\Phi_0} \Phi_{JJi} \right) + \alpha E_J \cos \left(\frac{2\pi}{\Phi_0} \left\{ \sum_{i=1}^{N} \Phi_{JJi} + \Phi_{ext} \right\} \right). \end{aligned} \tag{4.2}$$

Fluxoid quantization has been taken into account to write $\Phi_{JJ\alpha}$ as a function of the rest of magnetic fluxes. The conjugate momenta $q_i = \frac{\partial \mathcal{L}}{\partial \dot{\Phi}_i}$ are defined in Eq. (A.1), where $C_{eq} = \alpha C_J + C_{sh}$. Therefore, the matrix can be inverted for every N to obtain the functions $\dot{\mathbf{\Phi}}(\mathbf{q})$, which correspond to Eqs. (A.2), and then they can be substituted in the Legendre transformation Eq. (3.3) to obtain the Hamiltonian:

$$\begin{aligned} \mathcal{H} = T(\mathbf{q}) + U(\mathbf{\Phi}) = \frac{1}{2C_J} \sum_{i=1}^{N} q_{JJi}^2 - \frac{1}{2C_{eq} \left(\frac{C_J}{C_{eq}} + N \right)^2} \left(\sum_{i=1}^{N} q_{JJi} \right)^2 \\ - \sum_{i=1}^{N} E_J \cos \left(\frac{2\pi}{\Phi_0} \Phi_{JJi} \right) - \alpha E_J \cos \left(\frac{2\pi}{\Phi_0} \left\{ \sum_{i=1}^{N} \Phi_{JJi} + \Phi_{ext} \right\} \right), \end{aligned} \tag{4.3}$$

where $T(\mathbf{q})$ is the equivalent of the kinetic energy and $U(\mathbf{\Phi})$ the equivalent of the potential energy. The in-depth deduction can be found in Appendix A.1. With the relations obtained there, this same Hamiltonian could have been constructed as the sum of the contribution of every circuit element, which are described at Section 3.2, and taking into account fluxoid quantization.

4.1.1 *The double-well potential and a necessary condition for a N-Josephson Junction Flux Qubit*

Due to the Josephson Junction terms of the Hamiltonian, its potential is intricate. Nevertheless, when Φ_{ext} is near $\Phi_0/2$ the potential energy $U(\mathbf{\Phi})$ becomes a double-well (see Figure 4.2) along a defined path of the potential hypersurface. When the Hamiltonian is diagonalized, the two states with lower energy of the computational basis $\{|0\rangle, |1\rangle\}$ correspond to linear combinations of wavefunctions situated on the left and right wells $\{|L\rangle, |R\rangle\}$. The entire circuit can be therefore modeled as a two-level system and act as a qubit. Moreover, the basis of the wells corresponds to current circulating clockwise or counterclockwise and, therefore, can be directly measured.

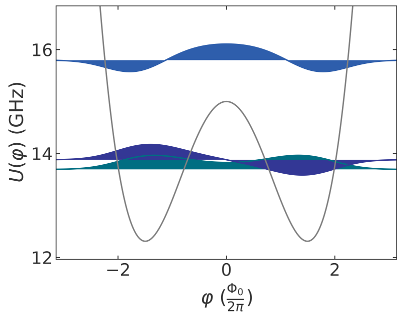

(a) $\Phi_{ext} = \Phi_0/2$.

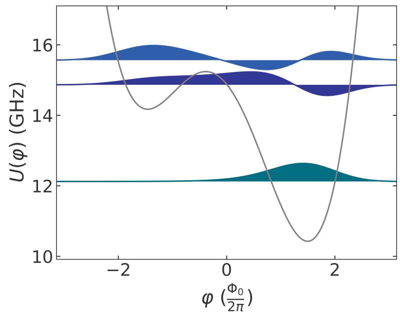

(b) Tilted potential ($\Phi_{ext} = 0.52 \cdot \Phi_0$).

Figure 4.2: Double-well potential and wavefunctions of the first eigenstates. Achieved with the simulation of a typical 3-Josephson Junction Qubit. Obtained with code from A.2.

This section proves one general necessary geometric condition for a double well to exist. The potential minima satisfies $\frac{\partial(U/E_J)}{\partial \Phi_i} = 0$. Taking $\Phi_{ext} = \Phi_0/2$ and considering the semi-classical approximation where phases are scalar variables, then the following expression must be true: $-\sin\varphi_i + \alpha \sin\sum_{i=1}^{N}\varphi_i = 0$.

Since this equality must be satisfied for each big Josephson Junction, then at the minima of the potential all the fluxes are equal $\varphi_i = \varphi^*$. Using the fact that Chebyshev polinomials of degree $N-1$ satisfy equation $\sin(Nx) = \sin(x)U_{N-1}(\cos(x))$, then the minima condition equals to $U_{N-1}(\cos\varphi^*) = \frac{1}{\alpha}$. In the interval between $[-1, 1]$, $U_{N-1}(x)$ takes the value N as its maximum value at $x = 1$, as proven in [39]. Therefore, because of the range of the cosine, the minima condition becomes $\frac{1}{N} < \alpha$. This sets a geometric condition that the circuit must abide in order to be able to obtain a double-well potential.

4.2 THE RF-SQUID

This section contains the first superconducting circuit of this thesis that has been used as a qubit. The results shown are widely known and, therefore, this section serves as a starting point from which the circuit's properties will be enhanced in later sections.

Historically, one of the first candidates of a superconducting qubit was the RF-SQUID. Invented in 1964 and presented in 1967 by Silver and Zimmerman [40], the RF-SQUID consists of a Josephson Junction shunted by a large inductance. In other words, a RF-SQUID corresponds to the circuit diagram 4.1a with $N = 0$ and an inductance instead of a chain of big junctions. Therefore, its Hamiltonian corresponds to $\widehat{\mathcal{H}} = \frac{\widehat{q}_L^2}{2C_{eq}} + \frac{\widehat{\Phi}_L^2}{2L} - E_J \cos\left(\frac{2\pi}{\Phi_0}\left\{\widehat{\Phi}_L + \Phi_{ext}\right\}\right)$, which is derived from Eq. (4.3) and where the index and ratio α have been dropped because there is only one type of Josephson Junction. The detailed deduction is in the Annex A.2.

Due to the high sensitivity to magnetic fluxes, the RF-SQUID has a broad range of applications in the biomedic field [41] and in magnetic property measurement systems [42]. Nevertheless, for Quantum Computing it has been proven to show some limitations. To maintain a double-well potential, large Josephson energies E_J must be achieved. To achieve a high enough E_J, a large inductance of the qubit loop is needed. Therefore, using conventional superconductors, the superconducting loop requires a relatively big area, which makes the qubit more sensitive to the environment and reduces its coherence time [26]. This drawback can be solved using additional Josephson Junctions as inductors instead of geometric inductors, thus reducing the susceptibility to noise. This change motivated the creation of the 3-Josephson Junction Flux Qubit [43] and, later on, the Fluxonium [44].

4.3 3JJ FLUX QUBIT WITH TUNABLE ASYMMETRIC X LOOP

This section describes a circuit which achieves longer coherence times than the RF-SQUID. Starting from the widely studied 3-Josephson Junction circuit, this thesis implements an equivalent asymmetry model to the one in [45], expanding the study of this effect. Moreover, we then find the main decoherence mechanism via simulations in *ScQubits* and optimize the parameters of the circuit in order to obtain longer coherence times.

The flux qubit was first studied by Orlando *et al.* [21]. It is formed by four Josephson Junctions (see Figure 4.3): c and d form a closed loop (X-loop), which behaves as an effective α-Junction, and a and b close the other loop (Z-loop). External fluxes (Φ_x, Φ_z) are thread to tune the properties of the system.

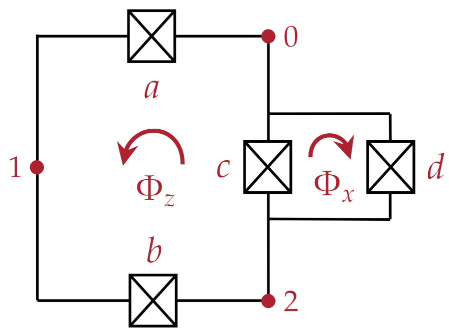

Figure 4.3: Diagram of a 3 Josephson Junction Flux Qubit.

The Z asymmetry would be equivalent to a circuit with additional α and α′ Josephson Junctions. This would result in a potential with more asymmetric minima.

To later simplify the potential to obtain an expression similar to the RF-SQUID, it is useful to utilize the critical currents $\alpha I_{a,b} = (I_c + I_d)/2$. Considering the asymmetry ratio of the X loop $\gamma_x = \frac{I_c}{I_d} = \frac{E_{Jc}}{E_{Jd}}$ then $E_{Jc} = \frac{2\alpha\gamma_x}{1+\gamma_x}E_J$ and $E_{Jd} = \frac{2\alpha}{1+\gamma_x}E_J$ with $E_J = E_{Ja} = E_{Jb}$. The Josephson Junctions of the Z loop could also be asymmetric, but its effect would only appear as a scaling factor before the corresponding cosine term in the potential. The 3-Junction Qubit potential can be found by adding the contributions of each circuit element. Using flux quantization, some trigonometry and a change of variables, the following potential is obtained:

$$U(\varphi) = -E_J\Bigg[\cos(\varphi_1) + \cos(\varphi_2') + 2\alpha\mathcal{A}\cos\left(\frac{\varphi_x}{2}\right)\times \cos\left(\varphi_2' - \varphi_1 - \varphi_z + \frac{\varphi_x}{2} - \beta\right)\Bigg], \tag{4.4}$$

where the asymmetry is contained in $\mathcal{A} = \sqrt{1 + \left(\frac{\gamma_x - 1}{\gamma_x + 1}\right)^2 \tan^2\left(\frac{\varphi_x}{2}\right)}$ and in the phase offset $\beta = \operatorname{atan}\left(\left(\frac{\gamma_x-1}{\gamma_x+1}\right)\tan\left(\frac{\varphi_x}{2}\right)\right)$. $\varphi_x = \frac{2\pi}{\Phi_0}\Phi_x$ and $\varphi_z = \frac{2\pi}{\Phi_0}\Phi_z$ correspond to the reduced external fluxes. The intermediate steps can be found in A.3. Figure 4.4 corresponds to the graphical representation of the potential for the symmetric case $\gamma_x = 1$. Figure 4.4a showcases how a Z external flux of $\varphi_z = \pi$ produces a double-well potential, with its minima at the "bowtie" shaped forms, corresponding to the double well of Figure 4.2a. Figure 4.4b shows how the double-well can be tilted using $\varphi_x \neq 0$, similar to the one obtained in Figure 4.2a.

It is worth noticing that the argument of the last cosine contains both external fluxes in the form of $\varphi_x/2 - \varphi_z$. Because of the geometry of the system, the external fluxes are not separable and the flux of the X loop affects the working point of φ_z. This effect is known as **quantum crosstalk** and explains why a non-zero φ_x tilts the double-well in Figure 4.4b. From a practical point of view, this circuit could

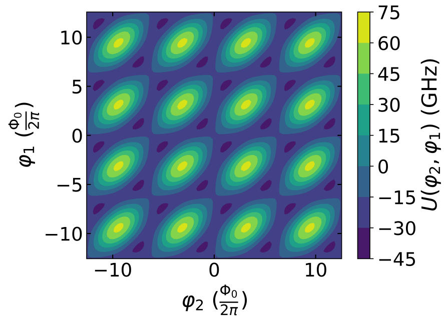

(a) $\varphi_x = 0$.

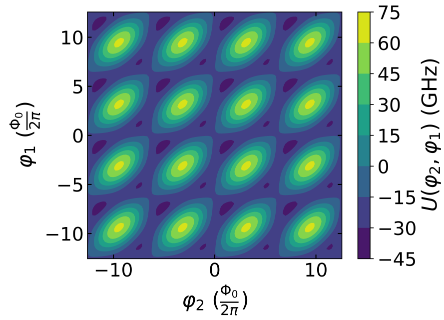

(b) $\varphi_x = 0.025 \cdot 2\pi$.

Figure 4.4: Potential energy of a 3 Josephson Junction Flux Qubit. The parameters used are $E_J/h = 20$ GHz, $\alpha = 0.6$, $\gamma_x = 1$ and $\varphi_z = \pi$. Obtained with A.3.

work as a tunable qubit, but quantum crosstalk would need to be corrected.

The external flux Φ_x additionally modifies the prefactor of the last cosine. This effect corresponds to the effective tuning of the α parameter, which translates into $\tilde{\alpha} = 2\alpha \cos\left(\frac{\varphi_x}{2}\right)$. When the asymmetry ratio $\gamma_x \neq 1$, then another dephasing β factor appears and the external flux of the X loop has an additional effect on the argument of the last cosine. Therefore, the effect of quantum crosstalk is accentuated in a nonlinear way. Moreover, because of the square root extra factor in $\mathcal{A}$, when the asymmetry γ_x is bigger, then the crosstalk effect is amplified due to a larger prefactor multiplying the last cosine, effectively producing $\tilde{\alpha}' = \mathcal{A}\tilde{\alpha}$.

For nearly symmetrical X loop Josephson Junctions ($\gamma_x \to 1$), a Taylor expansion of the potential until second order can be performed to yield:

$$
\begin{aligned}
U(\varphi) \approx -E_J \Bigg[\cos(\varphi_1) + \cos(\varphi_2') + 2\alpha \cos\left(\frac{\varphi_x}{2}\right) \\
\left(1 + \frac{\tan^2\left(\frac{\varphi_x}{2}\right)}{8}(\gamma_x - 1)^2\right) \cos\Bigg(\varphi_2' - \varphi_1 - \varphi_z + \frac{\varphi_x}{2} - \\
- \frac{\gamma_x - 1}{2} \tan\left(\frac{\varphi_x}{2}\right) + \frac{(\gamma_x - 1)^2}{4} \tan\left(\frac{\varphi_x}{2}\right)\Bigg)\Bigg].
\end{aligned}
\tag{4.5}
$$

Therefore, if the system starts to deviate from symmetry, the leading effect of asymmetry will be an extra phase on the cosine. For slightly more asymmetric loops, the next order effect will modify the prefactor of the cosine.

4.3.1 *Coherence time dependencies of the 3JJ Flux Qubit*

As said in section 3.3, the qubit relaxation time time is described by Fermi's Golden Rule (3.5). Since it depends on the inverse of $\Gamma_{i\to f}$, the maximization of the coherence time can be achieved trough the minimization of the off-diagonal matrix elements $\langle i|\mathcal{H}'|f\rangle$ or through the minimization of the noise power spectral density $S(\omega)$.

Starting with the minimization of $\langle i|\mathcal{H}'|f\rangle$, it is convenient to realize that, in an analogy to the harmonic oscillator Hamiltonian, the capacitance C of the Hamiltonians derived (like Eq. (4.3)) acts as the "mass" of the system. Therefore, shunting the system with higher capacitance localizes the eigensates at the minima as it can be seen in Figure 4.7a, thus reducing the first off-diagonal terms. Consequently, the coherence time is enhanced. Keeping in mind that E_C is inversely proportional to C, then a higher capacitance produces a higher ratio of energies E_J/E_C. The effect of capacitive shunting can be seen in Figure 4.5b. This result is also valid for Fluxoniums (see Sec. 4.4) and has been applied in [46] with *heavy Fluxoniums* obtaining coherence times of the order of the ms. One of the drawbacks of this method is the loss of anharmonicity in the qubit spectrum, which affects the qubit controlability.

To minimize the value of noise power spectral density $S(\omega)$, the predominant noise mechanism should be identified. It has been found, running simulations in *ScQubits* (Appendix A.4), that dielectric noise is the limiting factor for the 3-Junction Qubit. This noise is due to material imperfections and has been reported as a major limitation for phase qubits [47], transmons [48] and fluxoniums [49]. The first way to improve coherence time is to produce high quality dielectrics, through, for instance, enhanced cleaning methods in the clean room. *ScQubits* modelizes the spectral density of the dielectric noise as [50]:

$$S_{cap}(\omega) = \frac{2\hbar}{CQ_{\text{cap}}(\omega)}\left(\frac{\coth\frac{\hbar|\omega|}{2k_BT}}{1+\exp\left(-\frac{\hbar\omega}{k_BT}\right)}\right); Q_{\text{cap}}(\omega) = 10^6\left(\frac{2\pi\times 6}{|\omega|}\right)^{0.7}. \tag{4.6}$$

Using linear regressions in double log scales for the same simulations in *ScQubits*, it has been found that, near the double well limit, the effective coherence time is proportional to $t_{1\text{eff}}(\omega \ll 1) \propto \omega^{-0.7}$ and $t_{1\text{eff}}(\omega \gg 1) \propto \omega^{-1.7}$. The code used to find the exponents is shown in A.5. Therefore, lower qubit frequencies lead to longer coherence times. This can be achieved by decreasing E_J as in Figure 4.5a while, at the same time, increasing the energy ratio E_J/E_C as in Figure 4.5b.

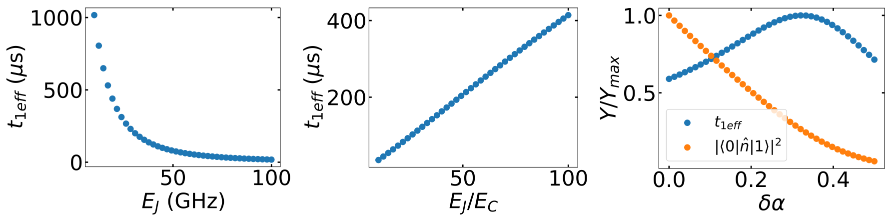

(a) $E_J/E_C = 100$. (b) $E_J = 20$ GHz. (c) $E_J = 20$ GHz and $E_J/E_C = 100$.

Figure 4.5: Effective relaxation time for the 3 Josephson Junction Qubit. Obtained with A.6, A.7 and A.8.

Another change that could be considered to improve the coherence time is to drive the qubit away from the double-well limit, thus modifying the matrix element of Fermi's Golden Rule formula. This is done by an increase of $\delta\alpha$ from $\alpha = \frac{1}{N}(1 + \delta\alpha)$. Figure 4.5c shows a maximum where the dielectric noise is minimized. From that point on, it is likely that another noise mechanism takes over and decreases the effective coherence time.

4.3.2 *Effects of the asymmetry on the potential*

It is also worth to study the dependence of the qubit frequency on the external fluxes. On the symmetric case ($\gamma_x = 1$), Figure 4.6a is obtained. There it can be seen how the linear crosstalk appears as periodic lines $\varphi_z - \varphi_x/2$ which correspond to the lower qubit gaps. This relation comes from the potential of the 3-Josephson Junction of Eq. (4.4). For the asymmetric case ($\gamma_x \neq 1$), Figure 4.6b is obtained where there are noticeable changes on the linearity, the slope and y-intercept due to the asymmetry parameters $\mathcal{A}$ and β.

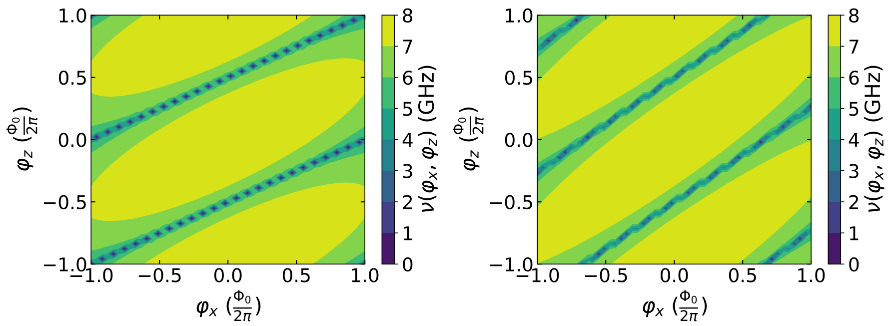

(a) Symmetric X loop $\gamma_x = 1$. (b) Asymmetric X loop $\gamma_x = 3$.

Figure 4.6: Qubit frequency as a function of external fluxes for the 3 Josephson Junction circuit with a symmetric and asymmetric X loop. The parameters used are $\alpha = 0.6$ and a ratio of energies E_J/E_C of 100. Obtained with A.9.

4.4 THE FLUXONIUM LIMIT

Continuing the work of the previous section, here we describe a circuit which achieves even longer coherence times via inductive shunting. It will be shown how, by addidion of a large number of big Josephson Junctions, the circuit achieves the Fluxonium limit. This work shows how the N-Josephson Junction Hamiltonian of Section 4.1 and the Fluxonium Hamiltonian proposed in the literature [46] produce the same results for $N \gg 1$. We also analyze the coherence time from simulations in *ScQubits* of circuits with different number of big Josephson Junctions.

The term Fluxonium was first coined by Manuchyaran *et al.* [44] and corresponds to a circuit of N Josephson Junctions with an α-Junction, corresponding to the diagram of Figure 4.1a. Even though Josephson Junctions are non-linear inductors, when the phase drop across them is low ($\varphi \ll 1$), they can be approximated to a linear inductor, resulting in the circuit diagram of Figure 4.1b. Therefore, a big enough array of N Josephson Junction with a big N and low Josephson Energy acts as an inductor of energy $E_L = (\Phi_0/2\pi)^2/(NL_J)$, with L_J the inductance of each Josephson Junction. This is the reason why the Hamiltonian of the Fluxonium is:

$$\widehat{\mathcal{H}} = 4E_C\widehat{N}^2 + \frac{1}{2}E_L\widehat{\varphi}^2 - E_J\cos\left(\widehat{\varphi} - \varphi_z\right), \tag{4.7}$$

where φ_z is the reduced external flux. The potential of the Fluxonium is represented in Figure 4.7 as well as the wavefunctions of the eigenstates with lower energy. The potential landscape of the fluxonium shows the characteristic multiple minima, which have been exaggerated for visual purposes. The double-well potential is obtained using a small Josephson Junction with its α near the limit found in Section 4.1.1 at $\varphi_z = \pi$.

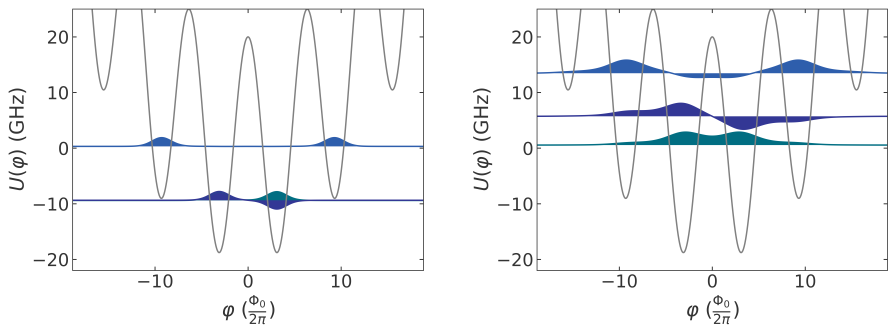

(a) *Heavy* fluxonium ($E_C/h = 2.5$ GHz). (b) Fluxonium ($E_C/h = 20$ GHz).

Figure 4.7: Fluxonium potential and wavefunctions of the first eigenstates. The parameters used are $E_J/h = 20$ GHz, $E_L/h = 0.25$ GHz and $\varphi_z = \pi$. Obtained with code from A.10.

An intuitive explanation behind the linear behavior of the array of N Josephson Junction in the Fluxonium limit is that, because of fluxoid quantization, the same total phase across the closed loop will have to be distributed across a bigger number of similar elements. Therefore, the phase drop for each element is reduced as more elements are introduced to the circuit. To check the equivalence between Hamiltonians, the flux drop corresponding to the inductor (or array of N Josephson Junctions) at the minimum corresponding to $\frac{\partial \hat{H}}{\partial \varphi} = 0$ must be the same for the two expressions. Therefore, near the double-well limit ($\alpha = 1.01/N$) Figure 4.8a is obtained where it can be seen that the values converge for $N > 20$.

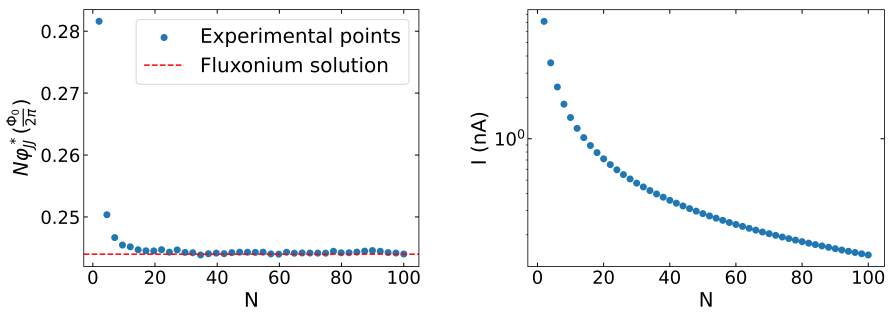

(a) Flux drop across the inductor with experimental points for N-Josephson Junction model and fluxonium solution from its Hamiltonian.

(b) Expected value of intensity of persistent current as a function of N Josephson Junction.

Figure 4.8: Flux drop and intensity of persistent current for the Fluxonium Qubit. Obtained with A.11 and A.12.

Formally, the condition for a big Josephson Junction to behave as a linear inductor is that its current must be much lower than its critical current I_C. In the Fluxonium case, the current decreases as N increases, as it can be seen in Figure 4.8b. This Figure has been obtained with *ScQubits* as the expectation value for the intensity operator and the ground state under the two-level approximation. The expectation value for the intensity operator corresponds to $\langle \hat{I} \rangle = \frac{\partial \langle \hat{\mathcal{H}} \rangle}{\partial \Phi_z}$ which, in this case, equals to $\langle \hat{I} \rangle = \frac{E_J}{N(1+\delta\alpha)} \frac{2\pi}{\Phi_0} \langle \sin(\hat{\varphi} - \pi) \rangle$.

4.4.1 *Coherence time of the Fluxonium Qubit*

Considering that the persistent current is low, Fluxoniums are less sensitive to noise. This is the reason why Fluxoniums achieve higher values of coherence time.

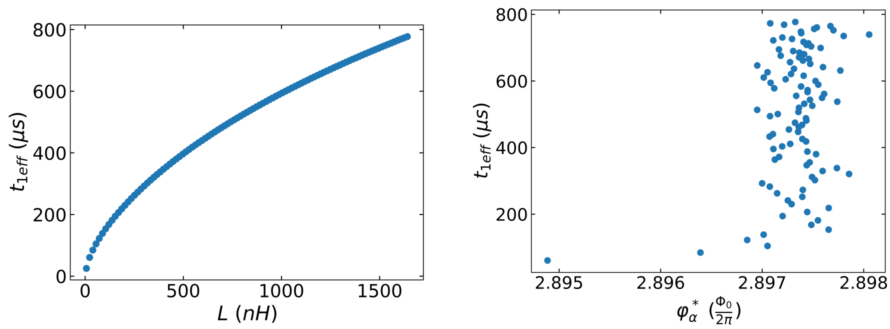

(a) Effective coherence time depending on the loop inductance and including dieletric noise.

(b) Effective coherence time depending on the phase drop across the α Josephson Junction.

Figure 4.9: Coherence time associated to the inductance and to the phase drop across the α-Junction. The parameters used for the big Josephson Junction are $E_J/h = 50$ GHz and $C_J = 2.5$ fF and $C_{sh} = 25$ fF. Obtained with codes A.13 and A.14.

Using *ScQubits*, different Fluxoniums have been simulated with different number of Josephson Junctions in the array, which are equivalent to inductances with different L. Therefore, Figure 4.9a clearly shows how a bigger inductance increases the effective coherence time. This effect is due to a better isolation between the first two qubit states, in a manner similar to Figure 4.7a with respect to Figure 4.7b but via direct modification of the potential.

The longer coherence time of the Fluxonium could be due to a lower phase drop across the α-Junction, which can be calculated as the position of the minimum of the double-well potential. Nevertheless, Figure 4.9b does not show a direct correlation between the effective coherence time and the phase drop across the α-Junction. The reason behind this could either be that it is not a variable which lets us tell apart Flux Qubits from Fluxoniums, non-neglegible computational error when the phase drop is computed or noise being independent of phase across the α-Junction.

4.5 GRADIOMETRIC FLUX QUBIT

The last circuit studied in this thesis is the Gradiometic Flux Qubit introduced in article [51], whose diagram corresponds to Figure 4.10. In this Section we study the Hamiltonian of the Gradiometric Flux Qubit using the same asymmetry model as in Sec. 4.3. It will be shown how this geometry makes the qubit capable of detecting differences between the external fluxes threading the two Z loops and suppresses linear quantum crosstalk. This thesis also shows conditions to obtain the double-well in this circuit and studies the effects that asymmetry has on it. Figure 4.10 shows a schematic of the circuit.

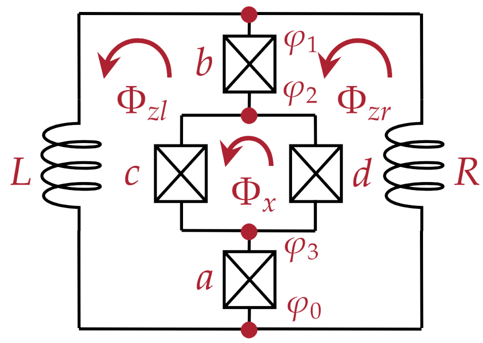

Figure 4.10: Diagram of a Gradiometric Flux Qubit.

For simplicity, the circuit will be considered symmetric with respect to the loop inductances $L_L = L_R = L/2$. To derive the potential energy it will be useful to first express the branch fluxes with their dependence on node fluxes as it has been done in Appendix A.4. It is worth to compute the addition and subtraction of the branch fluxes of the inductances. Therefore, with the inductor flux $\varphi_L = -\varphi_{zl} + \varphi_1$ and $\varphi_R = -\varphi_{zr} - \varphi_1 - \varphi_x$, then $\varphi_L - \varphi_R = \delta\varphi_z + \varphi_x + 2\varphi_1$ and $\varphi_L + \varphi_R = -\varphi_{zl} - \varphi_{zr} - \varphi_x$, which is the total external flux threading the circuit, with $\delta\varphi_z = \varphi_{zl} - \varphi_{zr}$. The inductive terms of the potential will be proportional to the sum of the square of the inductors fluxes and, thus, will be proportional to $\frac{1}{2}[(\varphi_{zr} + \varphi_{zl})^2 + (\varphi_{zr} - \varphi_{zl})^2]$. In this case, the term of the sum is equal to external fluxes and, therefore, will not be relevant in the dynamics of the system since they vanish when deriving the equations of motion. Therefore, the inductive terms will depend on the subtraction of the inductors phases, which corresponds to the second term. Using flux quantization, some trigonometry and changes of variables, the potential is obtained:

$$U(\varphi) = \frac{\Phi_0^2}{2L}\left(\frac{1}{2\pi}\right)^2 \varphi_1'^2 - E_J\Bigg[\cos(\varphi_3) + \cos(\varphi_2') + \\ +2\alpha\mathcal{A}\cos\left(\frac{\varphi_x}{2}\right)\cos\left(\frac{\varphi_1'}{2} - \frac{\delta\varphi_z}{2} - \varphi_2' - \varphi_3 - \beta\right)\Bigg], \tag{4.8}$$

where the definitions of the critical currents of subsection 4.3 have been applied to model the asymmetry of the X loop and the asymmetry appears in the prefactor $\mathcal{A} = \sqrt{1 + \left(\frac{\gamma_x - 1}{\gamma_x + 1}\right)^2 \tan^2\left(\frac{\varphi_x}{2}\right)}$ and the phase $\beta = \operatorname{atan}\left(\left(\frac{\gamma_x-1}{\gamma_x+1}\right)\tan\left(\frac{\varphi_x}{2}\right)\right)$.

It is worth to notice how, for a symmetric X loop $\gamma_x = 1$, the system does not show quantum crosstalk, contrary to the circuit in Sec. 4.3. Therefore, different parts of the Hamiltonian can be tuned independently using external magnetic fluxes φ_x and φ_z. The intermediate steps to obtain the potential are in the Annex A.4 and the same potential is verified in the Annex A.5. It is worth noticing that the non-linear crosstalk due to asymmetry remains identical to the non-gradiometric case of Eq. (4.4).

4.5.1 *Double well potential for the asymmetric gradiometric flux qubit*

In order to simplify the study of the potential and the double well regime, the following classical approximation is used: the system will stay close to the potential minima. This trick simplifies a multivariable potential to a single-variable function. Even though this approximation does not provide the exact values for the minima of the potential, it is useful to set constraints for the double well regime and to study qualitatively the potential. Therefore, the gradient corresponds to:

$$\nabla U(\varphi) = \begin{pmatrix} 2\frac{\Phi_0^2}{2L}\left(\frac{1}{2\pi}\right)^2\varphi_1' + \frac{1}{2}2\alpha E_J\cos\left(\frac{\varphi_x}{2}\right)\mathcal{A}\sin\left(\tilde{\beta}\right) \\ E_J\sin\left(\varphi_2'\right) - 2\alpha E_J\cos\left(\frac{\varphi_x}{2}\right)\mathcal{A}\sin\left(\tilde{\beta}\right) \\ E_J\sin\left(\varphi_3\right) - 2\alpha E_J\cos\left(\frac{\varphi_x}{2}\right)\mathcal{A}\sin\left(\tilde{\beta}\right) \end{pmatrix} = \vec{0}. \tag{4.9}$$

with $\tilde{\beta} = \frac{\varphi_1'}{2} - \frac{\delta\varphi_z}{2} - \varphi_2' - \varphi_3 - \beta$. By linear combination of the second and third elements, the minima condition imposes $\varphi = \varphi_2' = \varphi_3$. The number of variables can be reduced once more using the second relation $\varphi_1' = -\frac{E_J L}{2\Phi_0^2}(2\pi)^2\sin\varphi$, thus obtaining the single-variable potential:

$$\begin{aligned} U(\varphi) = \frac{LE_J^2}{8\Phi_0^2}\sin^2(\varphi) - E_J\Bigg[2\cos(\varphi) + 2\alpha\cos\left(\frac{\varphi_x}{2}\right)\mathcal{A}\times \\ \cos\left(\frac{E_J L}{4\Phi_0^2}(2\pi)^2\sin\varphi + 2\varphi + \frac{\delta\varphi_z}{2} + \beta\right)\Bigg]. \end{aligned} \tag{4.10}$$

We plot this potential in Figure 4.11. It is clear that $\delta\varphi_z = 2\pi$ will give rise to a double-well potential. For the symmetric case, to further study how to obtain an isolated double well potential, the single-variable potential can be expanded using $\delta\varphi_z = 2\pi$, obtaining:

$$U(\varphi) \approx \frac{LE_J^2}{8\Phi_0^2}\left(\varphi^2 - \frac{\varphi^4}{3}\right) - E_J\left[2\left(1 - \frac{\varphi^2}{2} + \frac{\varphi^4}{24}\right)\right.$$
$$\left. -2\alpha\cos\left(\frac{\varphi_x}{2}\right)\left(1 - \frac{1}{2}\left(\frac{E_J L}{4\Phi_0^2} + 2\right)^2\varphi^2 + \frac{1}{24}\left(\frac{E_J L}{4\Phi_0^2} + 2\right)^4\varphi^4\right)\right]. \tag{4.11}$$

After some algebra, for $\alpha > 1/\left(2\cos\left(\frac{\varphi_x}{2}\right)\left(\frac{E_J L}{4\Phi_0^2} + 2\right)\right)$ the quadratic terms will be positive and the terms raised to the fourth power will be positive. Therefore, this is the geometric constraint to obtain the double-well potential and it defines the type of potential caused by a given φ_x.

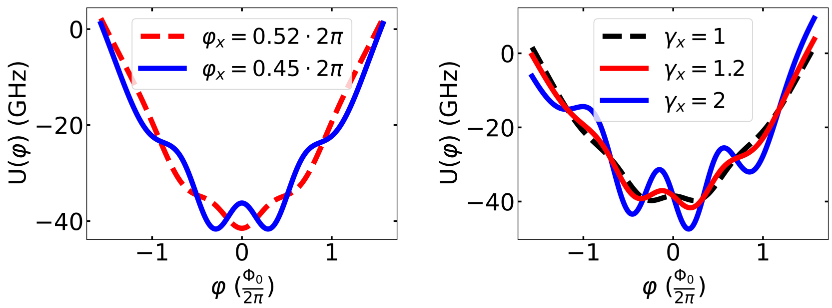

(a) $\delta\varphi_z = 2\pi$

(b) $\varphi_x = 0.45 \cdot 2\pi$, $\delta\varphi_z = 2\pi$

Figure 4.11: Potential for the asymmetric gradiometric circuit with $\nabla U = \vec{0}$, $\alpha = 0.6$, $E_J/h = 20$ GHz and $L = 250$ nH. Obtained with A.15 and A.16.

For $\varphi_x > \pi$ the cosine is negative and, since α can only be positive, there is no double well (see Figure 4.11a). For $\varphi_x = \pi$ the lower bound for α becomes ∞ and, therefore, the potential tends to $-\cos(x)$. Nevertheless, for $\varphi_x < \pi$ one could find a higher α than the positive and finite lower bound and, therefore, obtain a double well as in Figure 4.11a. Moreover, as the external flux φ_x is closer to π, the minima which are not from the double well start to disappear, thus isolating the double well.

In consequence, with the gradiometric geometry, the external fluxes decouple and quantum crosstalk disappears. Furthermore, it has been proven how the use of $\delta\varphi_z$ and φ_x can tune independently the potential energy. Nevertheless, real Josephson Junctions are not exactly equal and show some asymmetry. Since the asymmetry ratio γ_x between the Josepshon Energy of Josephson Junctions in the X loop appears in $\mathcal{A}$ and β, when $\varphi_X \neq 0$ then the asymmetry modifies the form of the potential (see Figure 4.11b). In this Figure, there is a dephasing effect due to β and other minima start reappearing. The prefactor $\mathcal{A}$ modifies the weight α of the last cosine and brakes the symmetric balance that existed between different terms of the potential.

Nowadays, the Josephson Junction defects of fabrication are of the order of 5%-10%. Therefore, in the worst case scenario $\gamma_x \approx 1.2$ the potential in Eq. (4.10) can be expanded with Taylor series around $\gamma_x - 1 \to 0$, thus obtaining Eq. (4.12) which is very similar to Eq. (4.5). The dephasing will be the first symptom of asymmetry, followed by an increase of the prefactor of the last cosine:

$$\begin{aligned} U(\varphi) \approx \frac{LE_J^2}{8\Phi_0^2}\sin^2(\varphi) - E_J \Bigg[2\cos(\varphi) + 2\alpha\cos\left(\frac{\varphi_x}{2}\right) \\ \left(1 + \frac{\tan^2\left(\frac{\varphi_x}{2}\right)}{8}(\gamma_x - 1)^2\right)\cos\left(\frac{E_J L}{4\Phi_0^2}(2\pi)^2\sin\varphi + 2\varphi + \frac{\delta\varphi_z}{2} + \right. \\ \left. + \frac{\gamma_x - 1}{2}\tan\left(\frac{\varphi_x}{2}\right) + \frac{(\gamma_x - 1)^2}{4}\tan\left(\frac{\varphi_x}{2}\right)\right)\Bigg]. \end{aligned} \tag{4.12}$$

Thus, the effect of quantum crosstalk reappears in the gradiometric potential as a consequence of asymmetry. Nevertheless, it is worth noticing how the non-linear crosstalk of Eq. (4.12) due to asymmetry is much smaller than the linear crosstalk of Eq. (4.5) due to the non-gradiometric geometry of the usual qubit.

4.6 POSSIBLE CONTINUATION OF THIS WORK

The circuits studied in this Chapter display enhanced properties compared to the RF-SQUID. Therefore, the completion of this work consists in the combination of the best features in one single circuit: the Gradiometric Fluxonium Qubit. This possible circuit would contain high capacitance and inductance values, which would shunt the circuit and, in consequence, increase the coherence time. As it has been shown, the gradiometric geometry would vanish the linear quantum crosstalk effect, improving the controlability of the circuit. Nevertheless, a more in-depth study should be performed in order to confirm these predictions.

5 CONCLUSIONS

This work has introduced superconducting qubits, as well as the theory needed to study and understand them. Circuit QED Theory has been used to obtain the Hamiltonian of different circuits.

The circuits have been introduced and studied, highlighting their advantages and disadvantages. The properties introduced and highlighted are coherence time, quantum crosstalk and junction asymmetry. Each circuit has presented an improvement in at least one of these properties.

For the 3-Josephson Junction Qubit, capacitive noise was found to be the predominant decoherence mechanism. Therefore, strategies have been presented as a way to increase the coherence time of the qubit. For a high value of N, it has been explained how a N-Josephson Junction circuit reaches the Fluxonium limit. There, it has been shown how a higher inductance significantly increases the coherence time. For the Gradiometric Qubit, it has been shown how, by construction, a symmetric circuit does not present linear quantum crosstalk.

For all of the circuits studied, conditions to obtain the double-well potential have been detailed. For the Gradiometric Qubit the effects of external fluxes in the form of the potential have been studied with more detail. Simulations have been performed with *ScQubits* that estimate coherence times and different Figures have been elaborated showcasing the effects of junction asymmetry on the potential, the frequency of the qubit and coherence times. The effects of low asymmetry on the potential have been derived, finding how it appears as a phase offset inside a cosine term of the potential and how it modifies the parameter α, giving rise to other local minima.

The completion of this work results in the fact that one could consider the collective set of enhancements in a single circuit: the Gradiometric Fluxonium Qubit, to be studied in future works.

APPENDIX A

A.1 IN-DEPTH DEDUCTION OF THE NJJ HAMILTONIAN

Given the following relation:

$$\mathbf{q} = \left(\frac{\partial \mathcal{L}}{\partial \dot{\mathbf{\Phi}}}\right) = C_{eq} \begin{pmatrix} 1+\frac{C_J}{C_{eq}} & 1 & \dots & 1 \\ 1 & 1+\frac{C_J}{C_{eq}} & \dots & 1 \\ \vdots & \vdots & \ddots & 1 \\ 1 & 1 & 1 & 1+\frac{C_J}{C_{eq}} \end{pmatrix} \begin{pmatrix} \dot{\Phi}_{JJ1} \\ \dot{\Phi}_{JJ2} \\ \vdots \\ \dot{\Phi}_{JJN} \end{pmatrix}. \tag{A.1}$$

Inverting the relation and obtaining $\mathbf{\Phi}(\mathbf{q})$:

$$\begin{pmatrix} \dot{\Phi}_{JJ1} \\ \dot{\Phi}_{JJ2} \\ \vdots \\ \dot{\Phi}_{JJN} \end{pmatrix} = \frac{1}{C_{eq}} \begin{pmatrix} 1+\frac{C_J}{C_{eq}} & 1 & \dots & 1 \\ 1 & 1+\frac{C_J}{C_{eq}} & \dots & 1 \\ \vdots & \vdots & \ddots & 1 \\ 1 & 1 & 1 & 1+\frac{C_J}{C_{eq}} \end{pmatrix}^{-1} \begin{pmatrix} q_{JJ1} \\ q_{JJ2} \\ \vdots \\ q_{JJN} \end{pmatrix}$$

$$\begin{pmatrix} \dot{\Phi}_{JJ1} \\ \dot{\Phi}_{JJ2} \\ \vdots \\ \dot{\Phi}_{JJN} \end{pmatrix} = \frac{1}{C_J\left(\frac{C_J}{C_{eq}}+N\right)} \begin{pmatrix} \left(\frac{C_J}{C_{eq}}+N-1\right) & -1 & \dots & -1 \\ -1 & \left(\frac{C_J}{C_{eq}}+N-1\right) & \dots & -1 \\ \vdots & \vdots & \ddots & -1 \\ -1 & -1 & -1 & \left(\frac{C_J}{C_{eq}}+N-1\right) \end{pmatrix} \begin{pmatrix} q_{JJ1} \\ q_{JJ2} \\ \vdots \\ q_{JJN} \end{pmatrix}. \tag{A.2}$$

Therefore, $\dot{\Phi}_{JJi} = \frac{1}{C_J}\left(q_i + \frac{q_\alpha}{\frac{C_J}{C_{eq}}+N}\right)$ where the variable $q_\alpha := -\sum_{i=1}^{N} q_i$ has been defined for commodity. Then, with the Legendre transformation of Eq. (3.3):

$$\begin{aligned}\mathcal{H} = \sum_{i=1}^{N} \dot{\Phi}_i q_i - \mathcal{L} = \sum_{i=1}^{N} \dot{\Phi}_i C_{eq}\left(\frac{C_J}{C_{eq}}\dot{\Phi}_i - \dot{\Phi}_\alpha\right) - \mathcal{L} = \frac{C_J}{2}\sum_{i=1}^{N}\dot{\Phi}_i^2 + \frac{C_{eq}}{2}\dot{\Phi}_\alpha^2 + U(\mathbf{\Phi}) \\ = \frac{1}{2C_J}\sum_{i=1}^{N}\left(q_i + \frac{q_\alpha}{\frac{C_J}{C_{eq}}+N}\right)^2 + \frac{C_{eq}}{2C_J^2}\left(\sum_{i=1}^{N} q_i + \frac{q_\alpha}{\frac{C_J}{C_{eq}}+N}\right)^2 + U(\mathbf{\Phi}).\end{aligned}$$

With some algebra, the following Hamiltonian is obtained:

$$\mathcal{H} = \frac{1}{2C_J}\sum_{i=1}^{N} q_{JJi}^2 - \frac{1}{2C_{eq}\left(\frac{C_J}{C_{eq}}+N\right)^2}\left(\sum_{i=1}^{N} q_{JJi}\right)^2 + U(\mathbf{\Phi}).$$

From the first steps of the derivation of the Hamiltonian, it is clear that it corresponds to the sum of the contributions from the N and α-Junction (with the C_{sh} correction to the capacitive term of α).

A.2 IN-DEPTH DEDUCTION OF THE RF-SQUID HAMILTONIAN

This circuit only contains two nodes which are allocated between the inductor and the JJ. Therefore, conservation of current corresponds to Eq. (A.3):

$$\frac{\Phi_L}{L} = -(C_{sh}-C)\ddot{\Phi}_L + I_c \sin\left(\varphi_L + \varphi_{ext}\right). \tag{A.3}$$

Which corresponds to the Lagrangian of Eq. (A.4):

$$\mathcal{L} = \frac{C_{eq}}{2}\dot{\Phi}_L^2 - \frac{1}{2L}\Phi_L^2 + E_J \cos\left(\varphi_L + \varphi_{ext}\right). \tag{A.4}$$

Then the canonically conjugate variable is $q_L = \frac{\partial \mathcal{L}}{\partial \dot{\Phi}_L}$ and, with the Legendre transform, the Hamiltonian (A.5) is obtained:

$$\mathcal{H} = \frac{q_L^2}{2C_{eq}} + \frac{\Phi_L^2}{2L} - E_J \cos\left(\frac{2\pi}{\Phi_0}\left\{\Phi_L + \Phi_{ext}\right\}\right). \tag{A.5}$$

Promoting the variables to operators, then the final Hamiltonian for the RF-SQUID is obtained.

A.3 INTERMEDIATE STEPS TOWARDS 3-JOSEPHSON JUNCTION POTENTIAL

Setting the ground to node 0 and substituting the branch fluxes by the nodes, the potential (A.6) is obtained:

$$\begin{aligned} U(\varphi) = -\sum_i E_{Ji}\cos\left(\varphi_i\right) = -E_J\Big[&\cos\left(\varphi_1\right) + \cos\left(\varphi_2 - \varphi_1 + \varphi_z\right) + \\ &+ \frac{2\alpha}{1+\gamma_x}\left\{\gamma_x \cos\left(-\varphi_2\right) + \cos\left(\varphi_2 + \varphi_x\right)\right\}\Big]. \end{aligned} \tag{A.6}$$

where flux quantization has been taken into account in the closing branches and $\varphi_x = \frac{2\pi}{\Phi_0}\Phi_x$ and $\varphi_z = \frac{2\pi}{\Phi_0}\Phi_z$ correspond to the reduced external flux. Performing the change of variable $\varphi_2' = \varphi_2 - \varphi_1 + \varphi_z$ and applying the formula for the cosine of the sum and subtraction of angles $\cos(\alpha \pm \beta) = \cos(\alpha)\cos(\beta) \mp \sin(\alpha)\sin(\beta)$, the potential (A.7) is obtained:

$$U(\varphi) = -E_J\Bigg[\cos(\varphi_1) + \cos(\varphi_2') + 2\alpha\cos\left(\frac{\varphi_x}{2}\right)\Bigg\{\cos\left(\varphi_2 + \frac{\varphi_x}{2}\right) + \\ + \left(\frac{\gamma_x - 1}{\gamma_x + 1}\right)\tan\left(\frac{\varphi_x}{2}\right)\sin\left(\varphi_2 + \frac{\varphi_x}{2}\right)\Bigg\}\Bigg]. \tag{A.7}$$

In order to obtain a more simplified expression, the following trick must be performed. Knowing that the end result should have the structure $\mathcal{C}\cos(\alpha - \beta)$, then the subtraction expression can be utilized with $\alpha = \varphi_2 + \frac{\varphi_x}{2}$, $\mathcal{C}\cos(\beta) = 1$ and $\mathcal{C}\sin(\beta) = \frac{\gamma_x - 1}{\gamma_x + 1}\tan\left(\frac{\varphi_x}{2}\right)$, thus obtaining potential (4.4):

$$U(\varphi) = -E_J\Bigg[\cos(\varphi_1) + \cos(\varphi_2') + 2\alpha\cos\left(\frac{\varphi_x}{2}\right) \\ \sqrt{1 + \left(\frac{\gamma_x - 1}{\gamma_x + 1}\right)^2\tan^2\left(\frac{\varphi_x}{2}\right)}\cos\Bigg(\varphi_2' - \varphi_1 - \varphi_z + \frac{\varphi_x}{2} - \\ - \operatorname{atan}\left(\left(\frac{\gamma_x - 1}{\gamma_x + 1}\right)\tan\left(\frac{\varphi_x}{2}\right)\right)\Bigg)\Bigg]. \tag{A.8}$$

A.4 INTERMEDIATE STEPS TOWARDS THE GRADIOMETRIC QUBIT POTENTIAL

To derive the potential it will be useful to first express the branch fluxes with their dependence on node fluxes obtaining $\varphi_a = \varphi_3$, $\varphi_b = \varphi_1 - \varphi_2$, $\varphi_c = \varphi_2 - \varphi_3$, $\varphi_d = \varphi_x + \varphi_2 - \varphi_3$, $\varphi_L = -\varphi_{zl} + \varphi_1$ and $\varphi_R = -\varphi_{zr} - \varphi_1 - \varphi_x$, where flux quantization has been used across the three closed loops. It is useful to compute $\varphi_L - \varphi_R = \varphi_{zl} - \varphi_{zr} + \varphi_x + 2\varphi_1 = \delta\varphi_z + \varphi_x + 2\varphi_1$ and $\varphi_L + \varphi_R = -\varphi_{zl} - \varphi_{zr} - \varphi_x$, with $\delta\varphi_z = \varphi_{zl} - \varphi_{zr}$, in order to find the inductive terms of the potential. These will be proportional to $(\varphi_{zr}^2 + \varphi_{zl}^2)$ which is equal to $\frac{1}{2}[(\varphi_{zr} + \varphi_{zl})^2 + (\varphi_{zr} - \varphi_{zl})^2]$.

Adding again the contributions of each circuit element, the potential of the system will be of the form of Eq. A.9, where the definitions of the critical currents of section 4.3 have been applied to model the asymmetry of the X loop:

$$U(\varphi)=\frac{\Phi_0^2}{2L}\left(\frac{1}{2\pi}\right)^2(\delta\varphi_z+\varphi_x+2\varphi_1)^2-E_J\Big[\cos(\varphi_1-\varphi_2)+ \\ +\cos(\varphi_3)+\frac{2\alpha}{1+\gamma_x}\Big\{\gamma_x\cos(\varphi_2-\varphi_3)+\cos(\varphi_2-\varphi_3+\varphi_x)\Big\}\Big]. \tag{A.9}$$

Performing the first change of variables $\varphi_1'=2\varphi_1+\delta\varphi_z+\varphi_x$ and then $\varphi_2'=\frac{\varphi_1'}{2}-\frac{\delta\varphi_z}{2}-\frac{\varphi_x}{2}-\varphi_2$, the potential obtained corresponds to Eq. (A.10):

$$U(\varphi)=\frac{\Phi_0^2}{2L}\left(\frac{1}{2\pi}\right)^2\varphi_1'^2-E_J\Big[\cos(\varphi_3)+\cos(\varphi_2')+ \\ +\frac{2\alpha}{1+\gamma_x}\Big\{\gamma_x\cos\left(\frac{\varphi_1'}{2}-\frac{\delta\varphi_z}{2}-\frac{\varphi_X}{2}-\varphi_2'-\varphi_3\right) \\ +\cos\left(\frac{\varphi_1'}{2}-\frac{\delta\varphi_z}{2}+\frac{\varphi_X}{2}-\varphi_2'-\varphi_3\right)\Big\}\Big]. \tag{A.10}$$

With the cosine of the sum and the subtraction of angles and knowing that the simplified expression is of the form $\mathcal{C}\cos(\alpha-\beta)$, the final Hamiltonian of the system corresponds to Eq. 4.8 with $\mathcal{A}=\sqrt{1+\left(\frac{\gamma_x-1}{\gamma_x+1}\right)^2\tan^2\left(\frac{\varphi_x}{2}\right)}$ and the phase $\beta=\operatorname{atan}\left(\left(\frac{\gamma_x-1}{\gamma_x+1}\right)\tan\left(\frac{\varphi_x}{2}\right)\right)$.

A.5 VERIFICATION OF THE GRADIOMETRIC QUBIT POTENTIAL

Knowing that the potential depends only on $U(\varphi)$ and that the kinteic energy depends only on $T(\mathbf{q})$, then a potential is correct if it generates the φ-dependent terms in the equations of motion. Applying Kirchhoff's laws for the different nodes, the equations of motion obtained correspond to:

$$\begin{aligned} C_b\ddot{\Phi}_b+I_{Cb}\sin\varphi_b+C_c\ddot{\Phi}_c+I_{Cc}\sin\varphi_c&=C_d\ddot{\Phi}_d+I_{Cd}\sin\varphi_d\\ C_a\ddot{\Phi}_a+I_{Ca}\sin\varphi_a+C_c\ddot{\Phi}_c+I_{Cc}\sin\varphi_c&=C_d\ddot{\Phi}_d+I_{Cd}\sin\varphi_d\\ C_b\ddot{\Phi}_b+I_{Cb}\sin\varphi_b+\frac{\Phi_R}{L/2}&=\frac{\Phi_L}{L/2}\\ C_a\ddot{\Phi}_a+I_{Ca}\sin\varphi_a+\frac{\Phi_R}{L/2}&=\frac{\Phi_L}{L/2}. \end{aligned} \tag{A.11}$$

It is worth to notice how the inductors' terms appear always as a difference, showcasing how the potential depends on $\varphi_L-\varphi_R=\varphi_1'$. Applying the definitions and changes of variables described in section 4.5, then the potential derived would produce the φ-dependent terms of Eq. (A.11) under Euler-Lagrange formula. Therefore, the formula derived describes correctly the potential of the system.

A.6 CODE USED

The following fragments of code have been made and used to obtain all the Figures and results of Chapter 4. The fragment A.1 includes general definitions, functions and libraries. Therefore, it is needed as a preamble for the rest of the code. More specific functions are specified at the top of each fragment.

Listing A.1: General initialization of the code

```
import scqubits as scq
import sccircuitbuilder as sc
import numpy as np
import matplotlib.pyplot as plt
from scipy.optimize import fsolve, minimize

E = 1.6021766208E-19
Flux0 = 2.067833831E-15

def convert_J_toGHz(value):
return value / (6.62607E-25)

def convert_GHz_toJ(value):
return value * (6.62607E-25)

def I_C_from_E_J(E_J):
return E_J * 2 * np.pi/Flux0

def E_J_in_GHz_from_I_C(I_C):
return convert_J_toGHz(I_C * Flux0 /(2 * np.pi))

plt.tick_params(axis='x', bottom=True, top=True,
    direction='in', length=4, width=1)
plt.tick_params(axis='y', left=True, right=True,
    direction='in', length=4, width=1)

plt.rcParams.update({
        'font.size': 20,
        'axes.titlesize': 22,
        'axes.labelsize': 20,
        'xtick.labelsize': 18,
        'ytick.labelsize': 18,
        'legend.fontsize': 20
})
```

Listing A.2: Graphical representation of the double-well potential of the 3-Josephson Junction Flux Qubit.

```
def create_qubit_from_ratio_energies(big_E_J, ratio, alpha_displacement, N, flux = 0.5):
alpha = 1/N * (1 + alpha_displacement)
E_C = big_E_J / N * (1 + alpha_displacement) / ratio
qubit = scq.Fluxonium(EJ = big_E_J / N * (1 + alpha_displacement), EC = E_C, EL = big_E_J / N, flux = flux, cutoff=120)
return qubit

numcycles = 4
numpoints = 100
numperiods = 1
numpoints = 500

N = 2
EJ = 20
alpha_displacement = 0.5
ratio = 100
flux = 0.52

qubit = create_qubit_from_ratio_energies(EJ, ratio, alpha_displacement, N, flux)
grid1d = scq.core.discretization.Grid1d(-numperiods/2 * 2 * np.pi, numperiods/2 * 2 * np.pi, numpoints)

plt.figure(1)
test = qubit.plot_wavefunction([0, 1, 2], phi_grid = grid1d)

plt.xlim(-numperiods/2 * 2 * np.pi, numperiods/2 * 2 * np.pi)
plt.xlabel(r'$\varphi$ $(\frac{\Phi_0}{2\pi})$', fontsize=20)
plt.ylabel(r'$U(\varphi)$ (GHz)', fontsize=20)
plt.xticks(fontsize=18)
plt.yticks(fontsize=18)
plt.tick_params(axis='x', bottom=True, top=True, direction='in', length=4, width=1)
plt.tick_params(axis='y', left=True, right=True, direction='in', length=4, width=1)

ax = plt.gca()
ax.spines['top'].set_visible(True)
ax.spines['right'].set_visible(True)
ax.spines['left'].set_visible(True)
ax.spines['bottom'].set_visible(True)

plt.savefig("qubit_potential_test_tilt.png", dpi=900, bbox_inches='tight', pad_inches=0.1)
plt.show()
```

Listing A.3: Graphical representation of the potential of the 3-Josephson Junction Flux Qubit.

```
def potential_2(phi1, phi2, alpha, EJ, gamma, phix,
    deltaphiz):

value = - EJ * ( np.cos(phi1) + np.cos(phi2) + 2 * alpha
    * np.cos((2 * np.pi) * phix / 2) * np.sqrt(1 + ((
    gamma - 1)/(gamma + 1))**2 * (np.tan((2 * np.pi) *
    phix/2))**2) * np.cos(phi2 - phi1 - (2 * np.pi) *
    deltaphiz + (2 * np.pi) * phix / 2 - np.arctan((gamma
     - 1)/(gamma + 1) * np.tan((2 * np.pi) * phix/2)))  )

return value

numcycles = 4
numpoints = 100
EJ = 20
phi2s = np.linspace(-numcycles/2 * 2 * np.pi, numcycles/2
     * 2 * np.pi, numpoints)
phi1s = np.linspace(-numcycles/2 * 2 * np.pi, numcycles/2
     * 2 * np.pi, numpoints)

alpha = 0.6
gamma = 1
potential = []
phix = 0
deltaphiz = 0.5

for phi1 in phi1s:

temp_potential = []

for phi2 in phi2s:

value = potential_2(phi1, phi2, alpha, EJ, gamma, phix,
    deltaphiz)

temp_potential.append(value)

potential.append(temp_potential)

print(phi1)

phi2_data, phi1_data = np.meshgrid(phi2s, phi1s)
plt.figure(1)
plt.contourf(phi2_data, phi1_data, potential)
cbar = plt.colorbar()
cbar.set_label(r"$U(\varphi_2, \varphi_1)$ (GHz)")
plt.xlabel(r"$\varphi_2$ $(\frac{\Phi_0}{2\pi})$")
plt.ylabel(r"$\varphi_1$ $(\frac{\Phi_0}{2\pi})$")
plt.tick_params(axis='x', bottom=True, top=True,
    direction='in', length=4, width=1)
plt.tick_params(axis='y', left=True, right=True,
    direction='in', length=4, width=1)
plt.tight_layout()
plt.savefig("3JJ_gamma1_phix0.png", dpi=900, bbox_inches=
    'tight', pad_inches=0.1)
plt.show()
```

Listing A.4: Simulation to find the predominant noise mechanism.

```
def create_qubit_from_ratio_energies(big_E_J, ratio,
    alpha_displacement, N, flux = 0.5):
alpha = 1/N * (1 + alpha_displacement)
E_C = big_E_J / N * (1 + alpha_displacement) / ratio
qubit = scq.Fluxonium(EJ = big_E_J / N * (1 +
    alpha_displacement), EC = E_C, EL = big_E_J / N, flux
     = flux, cutoff=120)
return qubit

N= 2
EJ = 20
ratio = 100
alpha_displacement = 0.01


test_qubit = create_qubit_from_ratio_energies(EJ, ratio,
    alpha_displacement, N, 0.5)


test_qubit.plot_t1_effective_vs_paramvals(param_name='
    flux',
param_vals=np.linspace(-0.5, 0.5, 100),
scale=1e-3,
ylabel=r"$\mu s$");

test_qubit.plot_coherence_vs_paramvals(param_name='flux',
param_vals=np.linspace(-0.5, 0.5, 100),
scale=1e-3,
ylabel=r"$\mu s$");
```

Listing A.5: Power law between the effective relaxation time and the frequency of the qubit.

```
def create_qubit_from_ratio_energies(big_E_J, ratio,
    alpha_displacement, N, flux = 0.5):
alpha = 1/N * (1 + alpha_displacement)
E_C = big_E_J / N * (1 + alpha_displacement) / ratio
qubit = scq.Fluxonium(EJ = big_E_J / N * (1 +
    alpha_displacement), EC = E_C, EL = big_E_J / N, flux
     = flux, cutoff=120)
return qubit

N = 100
big_E_Js = np.linspace(20, 80, 50)
ratio = 100
alpha_displacement = 0.01
qubit_gaps = []
T_capacitives_flux_05 = []
T_1_effs_flux_05 = []

for big_E_J in big_E_Js:

flux_qubit = create_qubit_from_ratio_energies(big_E_J,
    ratio, alpha_displacement, N, 0.5)

eigenvals = flux_qubit.eigenvals(evals_count=2)
qubit_gap = eigenvals[1] - eigenvals[0]
qubit_gaps.append(qubit_gap)

T_capacitives_flux_05.append(flux_qubit.t1_effective(
    noise_channels=['t1_capacitive']))
T_1_effs_flux_05.append(flux_qubit.t1_effective())

y_1_data = np.array(T_1_effs_flux_05)
y_1_data *= 1/1000

y_cap_data = np.array(T_capacitives_flux_05)
y_cap_data *= 1/1000

slope2, interception2 = np.polyfit(np.log(qubit_gaps), np
    .log(y_cap_data/max(y_cap_data)), 1)
correlation_matrix = np.corrcoef(np.log(qubit_gaps), np.
    log(y_cap_data/max(y_cap_data)))
correlation_coefficient = correlation_matrix[0, 1]
r2_corrcoef = correlation_coefficient ** 2
print("t1cap power law {}".format(slope2))
print(r2_corrcoef)

print(50 * "-")

slope2, interception2 = np.polyfit(np.log(qubit_gaps), np
    .log(y_1_data/max(y_1_data)), 1)
correlation_matrix = np.corrcoef(np.log(qubit_gaps), np.
    log(y_1_data/max(y_1_data)))
correlation_coefficient = correlation_matrix[0, 1]
r2_corrcoef = correlation_coefficient ** 2
print("t1eff power law {}".format(slope2))
print(r2_corrcoef)
```

Listing A.6: Coherence time as a function of E_J.

```
def create_qubit_from_ratio_energies(big_E_J, ratio,
    alpha_displacement, N, flux = 0.5):
alpha = 1/N * (1 + alpha_displacement)
E_C = big_E_J / N * (1 + alpha_displacement) / ratio
qubit = scq.Fluxonium(EJ = big_E_J / N * (1 +
    alpha_displacement), EC = E_C, EL = big_E_J / N, flux
     = flux, cutoff=120)
return qubit

N= 2
big_E_J_start = 10
big_E_J_end = 100
big_E_Js = np.linspace(big_E_J_start, big_E_J_end, 100)
ratio = 100
alpha_displacement = 0.01

t1_effs = []

for big_E_J in big_E_Js:
qubit_test = create_qubit_from_ratio_energies(big_E_J,
    ratio, alpha_displacement, N, 0.5)
t1_effs.append(qubit_test.t1_effective())

np_t1_effs = np.array(t1_effs)/1000

plt.figure(2)
plt.scatter(big_E_Js, np_t1_effs)
plt.tight_layout()
plt.ylabel(r'$t_{1 eff}$ $(\mu$s)')
plt.xlabel(r'$E_J$ (GHz)')
plt.tick_params(axis='x', bottom=True, top=True,
    direction='in', length=4, width=1)
plt.tick_params(axis='y', left=True, right=True,
    direction='in', length=4, width=1)
plt.savefig("3JJ_cohtime_EJ.png", dpi=900, bbox_inches='
    tight', pad_inches=0.1)
plt.show()
```

Listing A.7: Coherence time as a function of E_J/E_C.

```
def create_qubit_from_ratio_energies(big_E_J, ratio,
    alpha_displacement, N, flux = 0.5):
alpha = 1/N * (1 + alpha_displacement)
E_C = big_E_J / N * (1 + alpha_displacement) / ratio
qubit = scq.Fluxonium(EJ = big_E_J / N * (1 +
    alpha_displacement), EC = E_C, EL = big_E_J / N, flux
     = flux, cutoff=120)
return qubit

N= 2
EJ = 20
ratio_start = 10
ratio_end = 100
ratios = np.linspace(ratio_start, ratio_end, 100)
alpha_displacement = 0.01

t1_effs = []

for ratio in ratios:
qubit_test = create_qubit_from_ratio_energies(EJ, ratio,
    alpha_displacement, N, 0.5)
t1_effs.append(qubit_test.t1_effective())

np_t1_effs = np.array(t1_effs)/1000

plt.figure(2)
plt.scatter(ratios, np_t1_effs)
plt.tight_layout()
plt.ylabel(r'$t_{1eff}$ $(\mu$s)')
plt.xlabel(r'$E_J/E_C$')
plt.tick_params(axis='x', bottom=True, top=True,
    direction='in', length=4, width=1)
plt.tick_params(axis='y', left=True, right=True,
    direction='in', length=4, width=1)
plt.savefig("3JJ_cohtime_ratio.png", dpi=900, bbox_inches
    ='tight', pad_inches=0.1)
plt.show()
```

Listing A.8: Coherence time as a function of the distance to the double well limit.

```
def create_qubit_from_ratio_energies(big_E_J, ratio,
    alpha_displacement, N, flux = 0.5):
alpha = 1/N * (1 + alpha_displacement)
E_C = big_E_J / N * (1 + alpha_displacement) / ratio
qubit = scq.Fluxonium(EJ = big_E_J / N * (1 +
    alpha_displacement), EC = E_C, EL = big_E_J / N, flux
     = flux, cutoff=120)
return qubit

N = 2
big_E_J = 20


ratio = 100
alpha_displacements = np.linspace(0, 0.5, 50)

T_1_effs_flux_05 = []
mat_elems_squared = []


for alpha_displacement in alpha_displacements:

flux_qubit = create_qubit_from_ratio_energies(big_E_J,
    ratio, alpha_displacement, N, 0.5)

T_1_effs_flux_05.append(flux_qubit.t1_effective())
n_matrix = flux_qubit.matrixelement_table('n_operator',
    evals_count=6)
mat_elems_squared.append(n_matrix[0][1] * n_matrix[0][1].
    conjugate())

print(mat_elems_squared)
print(qubit_gaps)


y_1_data = np.array(T_1_effs_flux_05)
y_1_data *= 1/1000

plt.figure(3)
plt.scatter(alpha_displacements, y_1_data/max(y_1_data),
    label=r"$t_{1 eff}$")
plt.scatter(alpha_displacements, mat_elems_squared/max(
    mat_elems_squared), label=r"$|\langle{0}|\hat{n}|1\
    rangle|^2$")
plt.tight_layout()
plt.ylabel(r'$Y/Y_{max}$')
plt.xlabel(r'$\delta\alpha$')
plt.tick_params(axis='x', bottom=True, top=True,
    direction='in', length=4, width=1)
plt.tick_params(axis='y', left=True, right=True,
    direction='in', length=4, width=1)
plt.legend()
plt.savefig("coherence_delta_alpha.png", dpi=900,
    bbox_inches='tight', pad_inches=0.1)
plt.show()
```

Listing A.9: Coherence time as a function of external fluxes for a symmetric and asymmetric 3-Josephson Junction Flux Qubit.

```
def create_qubit_from_ratio_energies_3JJasymmetric(
    big_E_J, ratio, alpha, gamma, phiX, phiZ):
alpha_tilla = 2 * alpha * np.cos(0.5 * phiX) * np.sqrt(1
    + ((gamma-1)/(gamma+1))**2 * (np.tan(0.5 * phiX))**2)

if alpha_tilla < 0.5:
print("Not in double well!")
print("Gamma:"+str(gamma))
print("Alpha:"+str(alpha))
print("PhiX:"+str(phiX))

E_C = alpha_tilla * big_E_J / ratio
qubit = scq.Fluxonium(EJ = big_E_J * alpha_tilla, EC =
    E_C, EL = big_E_J / 2, flux = -phiZ + 0.5 * phiX + np
    .arctan(((gamma-1)/(gamma+1))*np.tan(0.5*phiX)),
    cutoff=120)
return qubit

N = 2
big_E_J = 20
ratio = 100
phiXs = np.linspace(-1, 1, 50)
phiZs = np.linspace(-1, 1, 50)
alpha = 0.6
gamma = 3
qubit_gaps = []

for phiZ in phiZs:
temp_qubit_gaps = []
for phiX in phiXs:
flux_qubit =
    create_qubit_from_ratio_energies_3JJasymmetric(
    big_E_J, ratio, alpha, gamma, phiX, phiZ)

eigenvals = flux_qubit.eigenvals(evals_count=2)
qubit_gap = eigenvals[1] - eigenvals[0]
temp_qubit_gaps.append(qubit_gap)

qubit_gaps.append(temp_qubit_gaps)

phiX_data, phiZ_data = np.meshgrid(phiXs, phiZs)
plt.figure(1)
plt.contourf(phiX_data, phiZ_data, qubit_gaps)
cbar = plt.colorbar()
cbar.set_label(r"$\nu(\varphi_x, \varphi_z)$ (GHz)")
plt.xlabel(r"$\varphi_x$ $(\frac{\Phi_0}{2\pi})$")
plt.ylabel(r"$\varphi_z$ $(\frac{\Phi_0}{2\pi})$")
plt.tick_params(axis='x', bottom=True, top=True,
    direction='in', length=4, width=1)
plt.tick_params(axis='y', left=True, right=True,
    direction='in', length=4, width=1)
plt.tight_layout()
plt.savefig("asym_ext_fluxes.png", dpi=900, bbox_inches='
    tight', pad_inches=0.1)
plt.show()
```

Listing A.10: Potential of the Fluxonium and representation of the wavefunctions of the lowest eigenstates.

```
fluxonium = scq.Fluxonium(EJ = 20,
EC = 20,
EL = 0.25,
flux = 0.5,
cutoff = 110)

numperiods = 6
numpoints = 500


grid1d = scq.core.discretization.Grid1d(-numperiods/2 * 2
     * np.pi, numperiods/2 * 2 * np.pi, numpoints)


plt.figure(1)
test = fluxonium.plot_wavefunction([0, 1, 2], phi_grid =
    grid1d)

plt.xlim(-numperiods/2 * 2 * np.pi, numperiods/2 * 2 * np
    .pi)
plt.ylim(-22, 25)
plt.xlabel(r'$\varphi$ $(\frac{\Phi_0}{2\pi})$', fontsize
    =20)
plt.ylabel(r'$U(\varphi)$ (GHz)', fontsize=20)
plt.xticks(fontsize=18)
plt.yticks(fontsize=18)
plt.tick_params(axis='x', bottom=True, top=True,
    direction='in', length=4, width=1)
plt.tick_params(axis='y', left=True, right=True,
    direction='in', length=4, width=1)

ax = plt.gca()
ax.spines['top'].set_visible(True)
ax.spines['right'].set_visible(True)
ax.spines['left'].set_visible(True)
ax.spines['bottom'].set_visible(True)

plt.savefig("fluxonium_potential_20.png", dpi=900,
    bbox_inches='tight', pad_inches=0.1)
plt.show()
```

Listing A.11: Minima of the double well for the Fluxonium.

```
def func_to_minimize(phi, N, alpha):
return - N * np.cos(phi) + alpha * np.cos(N * phi)

def graph_sweep_N(Ns, phis, alpha):
fig, ax = plt.subplots()
ax.scatter(Ns, np.multiply(np.abs(phis), Ns), label="
    Experimental points")
plt.axhline(y=0.244, color='r', linestyle='--', label="
    Fluxonium solution")
plt.tick_params(axis='x', bottom=True, top=True,
    direction='in', length=4, width=1)
plt.tick_params(axis='y', left=True, right=True,
    direction='in', length=4, width=1)
plt.ylabel(r'$N\varphi_{JJ}^*(\frac{\Phi_0}{2\pi})$')
plt.xlabel(r'N')
plt.legend()
plt.tight_layout()
plt.savefig("fluxonium_minima_by_NJJ.png", dpi=900,
    bbox_inches='tight', pad_inches=0.1)

def sweep_N_with_alpha_close(init_N, end_N, num_N,
    alpha_displacement, threshold, start_point = 0.1,
    display_funcs = False, display_sweep_N = True,
    return_phis = False, display_phialpha = False):
Ns = np.linspace(init_N, end_N, num_N)
phis = []

for i in range(len(Ns)):

N = Ns[i]
alpha = 1 / N  * (1 + alpha_displacement)
result = minimize(func_to_minimize, start_point, args = (
    N, alpha) ,options={"disp":False})

if second_derivative(result.x, N, alpha) <= 0:
print("Maximum mistaken by minimum. Try changing starting
     point.")
break

if np.abs(derivative(result.x, N, alpha)) >= threshold:
print("The first derivative is higher than the threshold.
    ")
break

phis.append(result.x[0])

if display_funcs == True:
graph_func(result.x, result.fun, N, alpha)

if display_sweep_N == True:
graph_sweep_N(Ns, phis, alpha)

if display_phialpha == True:
graph_sweep_N_alpha(Ns, phis, alpha)

if return_phis == True:
return phis
```

Listing A.12: Expectation value of the Intensity of the Fluxonium as a function of N.

```
big_E_J = 20
Ns = np.arange(2, 102, 2)
alpha_displacement = 0.01
ratio = 100

eigvals = []
eigvals_full = []

for N in Ns:
qubit_test = create_qubit_from_ratio_energies(big_E_J,
    ratio, alpha_displacement, N, 0.5)

I_operator = convert_GHz_toJ(big_E_J) / N * (1 +
    alpha_displacement) * (2 * np.pi) / Flux0  *
    qubit_test.sin_phi_operator(alpha = 1.0, beta = - np.
    pi)

submatrix = np.array([[I_operator[0, 0], I_operator[0,
    1]],
[I_operator[1, 0], I_operator[1, 1]]])


errors.append(np.abs(submatrix[0][0] / submatrix[1][0]))
eigvals_full.append(scipy.linalg.eigvalsh(I_operator)[0])
eigvals.append(scipy.linalg.eigvalsh(submatrix)[1])

plt.figure(1)
plt.scatter(Ns, np.array(eigvals) * 1E9)
plt.tick_params(axis='x', bottom=True, top=True,
    direction='in', length=4, width=1)
plt.tick_params(axis='y', left=True, right=True,
    direction='in', length=4, width=1)
plt.xlabel(r"N")
plt.ylabel(r"I (nA)")
plt.tight_layout()
plt.savefig("fluxonium_intensity_by_scqfluxonium.png",
    dpi=900, bbox_inches='tight', pad_inches=0.1)
plt.show()
```

Listing A.13: Part I: Simulation of coherence time for the Fluxonium circuit.

```
def create_fluxonium_Cshunted(big_E_J, C_bigJJ, C_sh,
    alpha_displacement, N, flux = 0.5):
alpha = 1/N * (1 + alpha_displacement)
C_eq = (alpha * C_bigJJ + C_sh) * 1E-15
E_C = convert_J_toGHz(E**2 /(2 * C_eq))
qubit = scq.Fluxonium(EJ = big_E_J / N * (1 +
    alpha_displacement), EC = E_C, EL = big_E_J / N, flux
     = flux, cutoff=120)
return qubit

def sweep_N_with_alpha_close_tuned(Ns, alpha_displacement
    , threshold, start_point = 0.1, display_funcs = False
    , display_sweep_N = True, return_phis_alpha = False,
    display_phialpha = False):
phis = []

for i in range(len(Ns)):

N = Ns[i]
alpha = 1 / N  * (1 + alpha_displacement)

result = minimize(func_to_minimize, start_point, args = (
    N, alpha) ,options={"disp":False})

if second_derivative(result.x, N, alpha) <= 0:
print("Maximum mistaken by minimum. Try changing starting
     point.")
break

if np.abs(derivative(result.x, N, alpha)) >= threshold:
print("The first derrivative is higher than the threshold
    .")
break

phis.append(result.x[0])

if display_funcs == True:
graph_func(result.x, result.fun, N, alpha)

if display_sweep_N == True:
graph_sweep_N(Ns, phis, alpha)

if display_phialpha == True:
graph_sweep_N_alpha(Ns, phis, alpha)

if return_phis_alpha == True:
return np.pi - np.multiply(np.abs(phis), Ns)


C_bigJJ = 2.5
C_sh = 25
alpha_displacement = 0.01
Ns = np.arange(2, 504, 5)
print(Ns)


big_E_J = 50
```

Listing A.14: Part II: Simulation of coherence time for the Fluxonium circuit.

```
T_1_effs_flux_05 = []

for N in Ns:
test_qubit = create_fluxonium_Cshunted(big_E_J, C_bigJJ,
    C_sh, alpha_displacement, N, flux = 0.5)
T_1_effs_flux_05.append(test_qubit.t1_effective(flux=0))

y_data = np.array(T_1_effs_flux_05)
y_data *= 1/1000


Ls = np.zeros(len(Ns))

Ls = Ns * (Flux0/(2 * np.pi)) ** 2 / convert_GHz_toJ(
    big_E_J) * 1E9

print(Ls[0])

plt.figure(3)
plt.scatter(Ls, y_data)
plt.tight_layout()
plt.ylabel(r'$t_{1 eff}$ $(\mu s)$')
plt.xlabel(r'$L$ $(nH)$')
plt.tick_params(axis='x', bottom=True, top=True,
    direction='in', length=4, width=1)
plt.tick_params(axis='y', left=True, right=True,
    direction='in', length=4, width=1)
plt.savefig("fluxonium_t1eff_L.png", dpi=900, bbox_inches
    ='tight', pad_inches=0.1)
plt.show()

phis_alpha_min = sweep_N_with_alpha_close_tuned(Ns, 0.01,
     1E-4, 0.1, False, False, True, False)

plt.figure(4)
plt.scatter(phis_alpha_min[1:], y_data[1:])
plt.tight_layout()
plt.ylabel(r'$t_{1 eff}$ $(\mu s)$')
plt.xlabel(r'$\varphi^*_{\alpha}$ $ (\frac{\Phi_0}{2\pi})
    $')
plt.tick_params(axis='x', bottom=True, top=True,
    direction='in', length=4, width=1)
plt.tick_params(axis='y', left=True, right=True,
    direction='in', length=4, width=1)
plt.savefig("fluxonium_t1eff_varphi_alpha.png", dpi=900,
    bbox_inches='tight', pad_inches=0.1)
plt.show()
```

Listing A.15: Single-variable potential of asymmetric gradiometric qubit.

```
def potential_more_reduced_gradiometric(phi, L, alpha, EJ
    , gamma, phix, deltaphiz):
LSI = L * 1E-9

value = 1/convert_J_toGHz(Flux0 ** 2 / LSI) * EJ ** 2 / 8
     * (np.sin(phi)) ** 2 - EJ * (2 * np.cos(phi) + 2 *
    alpha * np.cos((2 * np.pi) * phix / 2) * np.sqrt(1 +
    ((gamma - 1)/(gamma + 1))**2 * (np.tan((2 * np.pi) *
    phix/2))**2) * np.cos(1/convert_J_toGHz(Flux0**2/LSI)
     * EJ /4 * (2 * np.pi) ** 2 * np.sin(phi) + (2 * np.
    pi) * deltaphiz / 2 + 2 * phi + np.arctan((gamma - 1)
    /(gamma + 1) * np.tan((2 * np.pi) * phix/2))))

return value

numcycles = 1

big_E_J = 20
L = 250

phiX1 = 0
phiX2 = 0
delta_phiZ1 = 0
delta_phiZ2 = 1

alpha = 0.6
gamma = 1.1

phis = np.linspace(-numcycles/2 * 2 * np.pi, numcycles/2
    * 2 * np.pi, 500)

potential = []
potential2 = []

for phi in phis:
potential2.append(potential_more_reduced_gradiometric(phi
    , L, alpha, big_E_J, gamma, phiX2, delta_phiZ2))
potential.append(potential_more_reduced_gradiometric(phi,
     L, alpha, big_E_J, gamma, phiX1, delta_phiZ1))

plt.figure(1)

plt.tick_params(axis='x', bottom=True, top=True,
    direction='in', length=4, width=1)
plt.tick_params(axis='y', left=True, right=True,
    direction='in', length=4, width=1)
plt.plot(phis, potential, linestyle='--', color='red',
    linewidth=2.5, label=r"$\delta \varphi_z = 0$")
plt.plot(phis, potential2, color = "b", linewidth=2.5,
    label=r"$\delta \varphi_z = 2\pi$")
plt.legend()
plt.xlabel(r"$\varphi$ $ (\frac{\Phi_0}{2\pi})$")
plt.ylabel(r"U$(\varphi)$ (GHz)")
plt.savefig("1Dpotential_test_1.png", dpi=900,
    bbox_inches='tight', pad_inches=0.1)
plt.show()
```

Listing A.16: Single-variable potential of asymmetric gradiometric qubit for different asymmetry values.

```
numcycles = 1

big_E_J = 20
L = 250

phiX = 0.48
delta_phiZ = 1

alpha = 0.6
gamma1 = 1
gamma3 = 1.2
gamma4 = 2
gamma5 = 5

phis = np.linspace(-numcycles/2 * 2 * np.pi, numcycles/2
    * 2 * np.pi, 500)

potential1 = []
potential3 = []
potential4 = []


for phi in phis:
potential1.append(potential_more_reduced_gradiometric(phi
    , L, alpha, big_E_J, gamma1, phiX, delta_phiZ))
potential3.append(potential_more_reduced_gradiometric(phi
    , L, alpha, big_E_J, gamma3, phiX, delta_phiZ))
potential4.append(potential_more_reduced_gradiometric(phi
    , L, alpha, big_E_J, gamma4, phiX, delta_phiZ))

plt.figure(1)

plt.tick_params(axis='x', bottom=True, top=True,
    direction='in', length=4, width=1)
plt.tick_params(axis='y', left=True, right=True,
    direction='in', length=4, width=1)
plt.plot(phis, potential1, linestyle='--', color='black',
     linewidth=2.5,  zorder=3, label=r"$\gamma_x = 1$")
plt.plot(phis, potential3, color = "red", linewidth=2.5,
     zorder=2, label=r"$\gamma_x = 1.2$")
plt.plot(phis, potential4, color = "blue", linewidth=2.5,
      zorder=1, label=r"$\gamma_x = 2$")
plt.legend()
plt.xlabel(r"$\varphi$ $ (\frac{\Phi_0}{2\pi})$")
plt.ylabel(r"U$(\varphi)$ (GHz)")
plt.savefig("1Dpotential_1_asyms.png", dpi=900,
    bbox_inches='tight', pad_inches=0.1)
plt.show()
```

BIBLIOGRAPHY

[1] A. Petrillo, F. D. Felice, R. Cioffi, and F. Zomparelli, "Fourth industrial revolution: current practices, challenges, and opportunities," in *Digital transformation in smart manufacturing* (InTech, Feb. 2018).

[2] G. E. Moore, "Cramming more components onto integrated circuits," Electronics **38**, 114–117 (1965).

[3] P. Benioff, "Quantum mechanical hamiltonian models of turing machines," Journal of Statistical Physics **29**, 515–546 (1982).

[4] D. P. DiVincenzo, "Two-bit gates are universal for quantum computation," Physical Review A **51**, 1015–1022 (1995).

[5] N. Gisin and R. Thew, "Quantum communication," Nat. Photon. **1**, 165–171 (2007).

[6] N. Gisin and R. Thew, "Quantum communication technology," Electronics Letters **46**, 965–967 (2010).

[7] I. M. Georgescu, S. Ashhab, and F. Nori, "Quantum simulation," Reviews of Modern Physics **86**, 153–185 (2014).

[8] A. J. Daley, I. Bloch, C. Kokail, S. Flannigan, N. Pearson, M. Troyer, and P. Zoller, "Practical quantum advantage in quantum simulation," Nature **607**, 667–676 (2022).

[9] F. Arute et al., "Quantum supremacy using a programmable superconducting processor," Nature **574**, 505–510 (2019).

[10] P. W. Shor, "Polynomial-time algorithms for prime factorization and discrete logarithms on a quantum computer," SIAM Journal on Computing **26**, 1484–1509 (1997).

[11] C. H. Bennett and G. Brassard, "Quantum cryptography: public key distribution and coin tossing," Theoretical Computer Science **560**, 7–11 (2014).

[12] A. K. Ekert, "Quantum cryptography based on bell's theorem," Phys. Rev. Lett. **67**, 661–663 (1991).

[13] V. Scarani, A. Acín, G. Ribordy, and N. Gisin, "Quantum cryptography protocols robust against photon number splitting attacks for weak laser pulse implementations," Phys. Rev. Lett. **92**, 057901 (2004).

[14] J. J. García-Ripoll, *Quantum information and quantum optics with superconducting circuits* (Cambridge University Press, 2022).

[15] D. Loss and D. P. DiVincenzo, "Quantum computation with quantum dots," Physical Review A **57**, 120–126 (1998).

[16] D. G. Cory, A. F. Fahmy, and T. F. Havel, "Ensemble quantum computing by nmr spectroscopy," Proceedings of the National Academy of Sciences **94**, 1634–1639 (1997).

[17] I. Bloch, J. Dalibard, and W. Zwerger, "Many-body physics with ultracold gases," Reviews of Modern Physics **80**, 885–964 (2008).

[18] H. Haffner, C. Roos, and R. Blatt, "Quantum computing with trapped ions," Physics Reports **469**, 155–203 (2008).

[19] S. Pezzagna and J. Meijer, "Quantum computer based on color centers in diamond," Applied Physics Reviews **8**, 011308 (2021).

[20] D. Castelvecchi, "Quantum-computing approach uses single molecules as qubits for first time," Nature (2023).

[21] T. P. Orlando, J. E. Mooij, L. Tian, C. H. van der Wal, L. S. Levitov, S. Lloyd, and J. J. Mazo, "Superconducting persistent-current qubit," Phys. Rev. B **60**, 15398–15413 (1999).

[22] L. Henriet, L. Beguin, A. Signoles, T. Lahaye, A. Browaeys, G.-O. Reymond, and C. Jurczak, "Quantum computing with neutral atoms," Quantum **4**, 327 (2020).

[23] B. Yurke and J. S. Denker, "Quantum network theory," Phys. Rev. A **29**, 1419–1437 (1984).

[24] M. H. Devoret, "Quantum Fluctuations in Electrical Circuits," in Fluctuations quantiques/quantum fluctuations, edited by S. Reynaud, E. Giacobino, and J. Zinn-Justin (Jan. 1997), p. 351.

[25] S. M. Girvin, "Circuit qed: superconducting qubits coupled to microwave photons," in *Quantum machines: measurement and control of engineered quantum systems* (Oxford University PressOxford, June 2014), pp. 113–256.

[26] G. Wendin and V. S. Shumeiko, "Superconducting quantum circuits, qubits and computing," arXiv:cond-mat/0508729 (2005).

[27] B. S. Deaver and W. M. Fairbank, "Experimental evidence for quantized flux in superconducting cylinders," Physical Review Letters **7**, 43–46 (1961).

[28] R. Doll and M. Näbauer, "Experimental proof of magnetic flux quantization in a superconducting ring," Physical Review Letters **7**, 51–52 (1961).

[29] A. Mizel, "Theory of superconducting qubits beyond the lumped-element approximation," Phys. Rev. Appl. **21**, 024030 (2024).

[30] B. Josephson, "Possible new effects in superconductive tunnelling," Physics Letters **1**, 251–253 (1962).

[31] P. W. Anderson and J. M. Rowell, "Probable observation of the josephson superconducting tunneling effect," Phys. Rev. Lett. **10**, 230–232 (1963).

[32] I. Giaever, "Energy gap in superconductors measured by electron tunneling," Physical Review Letters **5**, 147–148 (1960).

[33] T. P. Orlando and K. A. Delin, *Foundations of applied superconductivity*, en (Prentice Hall, Old Tappan, NJ, 1991).

[34] M. Tinkham, *Introduction to superconductivity: v. 1*, 2nd ed., Dover Books on Physics (Dover Publications, Mineola, NY, June 2004).

[35] B. H. Bransden and C. J. Joachain, *Quantum mechanics*, en, 2nd ed. (Prentice-Hall, London, England, Jan. 2000).

[36] P. A. M. Dirac, *The quantum theory of the emission and absorption of radiation*, edited by M. E. Noz and Y. S. Kim (Springer Netherlands, Dordrecht, 1988), pp. 157–179.

[37] E. Fermi, *Nuclear physics* (University of Chicago Press, Chicago, IL, Aug. 1974).

[38] S. Rasmussen, K. Christensen, S. Pedersen, L. Kristensen, T. Bækkegaard, N. Loft, and N. Zinner, "Superconducting circuit companion—an introduction with worked examples," PRX Quantum **2**, 1 (2021).

[39] O. Veselovska, V. Dostoina, and M. Klapchuk, "Properties of the second-kind chebyshev polynomials of complex variable," Researches in Mathematics **28**, 35 (2020).

[40] A. H. Silver and J. E. Zimmerman, "Quantum states and transitions in weakly connected superconducting rings," Physical Review **157**, 317–341 (1967).

[41] J. Clarke and A. I. Braginski, eds., *The SQUID handbook*, en, The SQUID Handbook (Wiley-VCH Verlag, Weinheim, Germany, Aug. 2006).

[42] R. Kleiner, D. Koelle, F. Ludwig, and J. Clarke, "Superconducting quantum interference devices: state of the art and applications," Proceedings of the IEEE **92**, 1534–1548 (2004).

[43] J. E. Mooij, T. P. Orlando, L. Levitov, L. Tian, C. H. van der Wal, and S. Lloyd, "Josephson persistent-current qubit," Science **285**, 1036–1039 (1999).

[44] V. E. Manucharyan, J. Koch, L. I. Glazman, and M. H. Devoret, "Fluxonium: single cooper-pair circuit free of charge offsets," Science **326**, 113–116 (2009).

[45] M. Khezri, J. A. Grover, J. I. Basham, S. M. Disseler, H. Chen, S. Novikov, K. M. Zick, and D. A. Lidar, "Anneal-path correction in flux qubits," npj Quantum Information **7**, 36 (2021).

[46] N. Earnest et al., "Realization of a λ system with metastable states of a capacitively shunted fluxonium," Physical Review Letters **120**, 150504 (2018).

[47] J. M. Martinis et al., "Decoherence in josephson qubits from dielectric loss," Physical Review Letters **95**, 210503 (2005).

[48] J. M. Martinis, "Surface loss calculations and design of a superconducting transmon qubit with tapered wiring," npj Quantum Information **8**, 26 (2022).

[49] L. B. Nguyen, Y.-H. Lin, A. Somoroff, R. Mencia, N. Grabon, and V. E. Manucharyan, "High-coherence fluxonium qubit," Physical Review X **9**, 041041 (2019).

[50] W. C. Smith, A. Kou, X. Xiao, U. Vool, and M. H. Devoret, "Superconducting circuit protected by two-cooper-pair tunneling," npj Quantum Information **6**, 8 (2020).

[51] F. G. Paauw, A. Fedorov, C. J. P. M. Harmans, and J. E. Mooij, "Tuning the gap of a superconducting flux qubit," Phys. Rev. Lett. **102**, 090501 (2009).